Synthesis of g-C_3N_4/Ba-ZnO Nanocomposites for Photocatalytic Degradation of Methylene Blue and Antibacterial Application

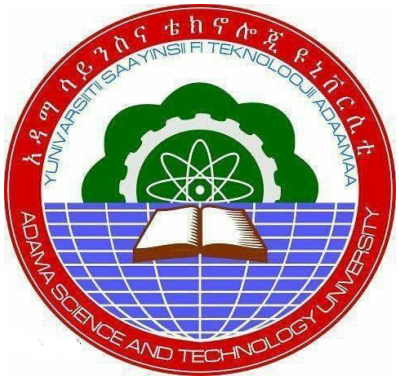

Daniel Shumi

A Thesis Submitted to

The Department of Applied Chemistry

School of Applied Natural Science

Presented in Partial Fulfillment of the Requirement for the Degree of Master of Science in Applied Chemistry (Industrial chemistry)

Office of Graduate Studies

Adama Science and Technology University

January 2023

Adama, Ethiopia

Synthesis of g-C_3N_4/Ba-ZnO Nanocomposites for Photocatalytic Degradation of Methylene Blue and Antibacterial Application

Daniel Shumi

Advisor: Aschalew Tadesse (PhD)

A Thesis Submitted to

The Department of Applied Chemistry

School of Applied Natural Science

Presented in Partial Fulfillment of the Requirement for the Degree of Master of Science in Applied Chemistry (Industrial chemistry)

Office of Graduate Studies

Adama Science and Technology University

January 2023

Adama, Ethiopia

Declaration

I hereby declare that this Master's Thesis entitled "Synthesis of g-C_3N_4/Ba-ZnO Nanocomposites for Photocatalytic Degradation of Methylene Blue and Antibacterial Application" is my original work and has not been submitted for the award of any academic degree, diploma or certificate in any other university. All sources of materials that are used for this thesis have been duly acknowledged through citation.

_____	_____	_____
Name of student	Signature	Date

Recommendation of Advisor

I the advisor of this thesis, hereby certify that I have read the revised version of the thesis entitled "Synthesis of g-C_3N_4/Ba-ZnO Nanocomposites for Photocatalytic Degradation of Methylene Blue and Antibacterial Application" prepared under my guidance by Daniel Shumi submitted in partial fulfillment of the requirements for the degree of Master of Science in Applied Chemistry. Therefore, I recommend the submission of a revised version of the thesis to the department following the applicable procedures.

_____	_____	_____
Major Advisor	Signature	Date

Approval Page

I, the advisor of the thesis entitled **"**Synthesis of g-C_3N_4/Ba-ZnO Nanocomposites for Photocatalytic Degradation of Methylene Blue and Antibacterial Application**"** and developed by Daniel Shumi hereby certify that the recommendation and suggestions made by the board of examiners are appropriately incorporated into the final version of the thesis.

_____	_____	_____
Major Advisor	Signature	Date

Approval of Board of Reviewers

We, the undersigned, members of the Board of Examiners of the thesis by Daniel Shumi have read and evaluated the thesis entitled "Synthesis of g-C_3N_4/Ba-ZnO Nanocomposites for Photocatalytic Degradation of Methylene Blue and Antibacterial Application" and examined the candidate during the open defense. This is, therefore, to certify that the thesis is accepted for partial fulfillment of the requirement of the degree of Master of Science in Applied Chemistry (Industrial chemistry).

Chairperson	Signature	Date
Internal Examiner	Signature	Date
External Examiner	Signature	Date

Final approval and acceptance of the thesis is contingent upon submission of its final copy to the Office of Postgraduate Studies (OPGS) through the Department Graduate Council (DGC) and School Graduate Committee (SGC).

Department Head	Signature	Date
School Dean	Signature	Date
Office of Postgraduate Studies, Dean	Signature	Date

Acknowledgment

First of all, I would like to thank the Almighty God for giving me health, patience, and strength throughout the entire challenge that I faced during my research work.

I would like also to express my deepest gratitude to my advisor Dr. Aschalew Tadesse for his useful suggestions, kind support, guidance, and valuable comments at the various stages of the thesis work and contributions of ideas as well as for sharing his precious time to read this thesis.

Then I would like to give honorable thanks to Adama Science and Technology University for giving me this scholarship program to endure my academic career. Furthermore, I would like to express my sincere gratitude to all academic, technical, and support staff of the Program of Applied Chemistry especially Mr. Guta Amenu and Mr. Lemi Bulto, for providing the necessary knowledge, assistance, and facilities to conduct my research work.

Finally, last but the least gratitude goes to my family and friends who were big sources of inspiration throughout my research work with their valuable moral support and advice.

Table of Contents

List of Tables

List of Figures

List of Abbreviations

g-CN	Graphitic carbon nitride
NPs	Nanoparticles
NMs	Nanomaterials
NCs	Nanocomposites
XRD	X-ray diffraction
UV	Ultraviolet
UV-DRS	Ultraviolet-visible diffuse reflectance spectra
FTIR	Fourier-transform infrared spectrometer
SEM	Scanning electron microscope
TEM	Transmission electron microscope
PCA	Photocatalytic activity
RhB	Rhodamine B
MB	Methylene blue
MO	Methyl orange
MG	Malachite green
VB	Valence band
CB	Conduction band
ROS	Reactive oxygen species

Executive Summary

Photocatalytic degradation is an effective method to reduce environmental pollution caused by organic pollutants. In this work, the photocatalytic and antibacterial activity of graphitic carbon nitride (g-C_3N_4) coupled with Barium doped zinc oxide (Ba-ZnO) composite material was studied. The polymeric g-C_3N_4 materials were fabricated by the pyrolysis of urea. ZnO and Ba-ZnO nanoparticles were produced by a coprecipitation method. More importantly, g-C_3N_4/Ba-ZnO nanostructured composites were fabricated by adding the different amounts of graphitic carbon nitride (10%, 20% 30%, 40%, 50%, 60%) into Ba-doped ZnO via the simple co-precipitation method. The fabricated materials were characterized by X-ray diffraction (XRD), UV–vis diffuse reflectance spectroscopy (UV-vis-DRS), Fourier transform infrared (FT-IR) spectroscopy, and scanning electron microscopy (SEM). XRD results have revealed that the ternary NC exhibited new peaks which evidenced the successful incorporation of Ba and g-C_3N_4. The incorporation of Ba and g-C_3N_4 into the ZnO matrix has shifted the absorption edge toward the visible region as observed in UV-DRS spectra. FTIR spectra manifested the presence of the characteristic absorption peak at $571\ cm^{-1}$ *of Zn–O bending vibrational modes confirming the target nanoparticles synthesis. The SEM images revealed random-shaped rough morphology for the NC with a clear influence of the presence of Ba and g-C_3N_4. All the fabricated nanomaterials were investigated for their photocatalytic activity by using methylene blue (MB) dye. Ternary NCs, in which 50% g-C_3N_4 hybridized with Ba-doped ZnO (g-C_3N_4/Ba-ZnO) NCs were proven to be optimum photocatalysts for the degradation of methylene blue (MB) dye under sunlight irradiation. Further, parameters such as the effect of pH of the dye solution, catalyst loading, and initial dye concentration were also studied and optimum degradation efficiencies were found at pH 9, 0.3 g catalyst loading, and 10 mg/L dye concentration. Moreover, the reusability of the recovered photocatalyst was studied efficiently up to 5 cycles in the degradation process. The synthesized photocatalysts were also applied against Gram-positive* (*S. aureus and S. pyogen*) *and Gram-negative* (*E. coli and P. aeruginosa*) *bacterial strains to evaluate their antibacterial activities. The antibacterial activity of the 50% g-C_3N_4/Ba-ZnO NC was compared to other synthesized nanomaterials and found to have better inhibition zone values against all studied bacterial strains.*

Keywords: Ba-doped ZnO nanoparticles, g-C_3N_4/Ba-ZnO nanocomposite, Photocatalytic degradation, antibacterial activity

1. Introduction

1.1 Background

In the twenty-first-century reliable access to clean water remains a major global challenge (Qu et al., 2013). Rapid population growth, enormous industrialization, enhancement of agricultural activities to meet food demand, other geological and environmental, and global changes have contributed to both the increased variety and volume of pollutants continuously contaminating the water sources (da Silva & Gouveia, 2020; Karimi-Maleh et al., 2019; Shamsadin-Azad et al., 2019). A large number of industries such as leather, paper, plastic, textile, food processing, printing, cosmetics, pharmaceuticals, etc., deal with dyes. The uncontrolled release of colored wastewater contaminated with dyes from these industries has led to serious environmental contamination (Pekakis et al., 2006). As these chemicals are stable to natural decomposition, their ever-increasing levels in the environment, specifically in water bodies, adversely affect the quality of water, inhibit sunlight penetration and reduce photosynthetic reactions. In addition, some dyes are either toxic or carcinogenic (Constapel et al., 2009). As a result, the quality of water sources for industrial, agricultural, and human consumption is worsening globally. Therefore, it is a timely need to develop suitable, inexpensive, and efficient treatment techniques for water purification (Ali et al., 2020).

Presently, conventional procedures such as sedimentation, filtration, chemical, and membrane technologies (Chong et al., 2010) have been employed to get rid of polluting dyes. Nevertheless, these classical processes face lots of drawbacks such as soaring cost and inefficiency. Alternatively, adsorption as a low-cost, efficient, and exceedingly effective technique for the elimination of organic dyes is highly appreciated (Verma et al., 2012; Zahrim & Hilal, 2013). Natural adsorbents such as clays, zeolites, and bentonite are employed in dye adsorption and removal (Ai et al., 2011). Alternatively, nanomaterials are recently employed to get rid of these hazardous dyes from water and wastewater system (Rehman, 2021). Nanomaterials are superior to natural catalysts of their photocatalytic activity associated with their bandgap as semiconductors (Ayodhya, 2019). To decrease the damage caused by organic dyes, studies have been focused on photocatalysts to convert organic dyes to harmless chemicals.

Photocatalytic degradation of toxic dyes by semiconductor oxides has been extensively studied and utilized because of its effectiveness as well as the non-toxicity of its byproducts (M. M. Khan

et al., 2015). The use of metal oxides semiconductor materials, such as TiO_2 and ZnO, as photocatalysts, has attracted much attention due to the ability of these materials to degrade pollutants under UV irradiation. Among these photocatalysts, zinc oxide is a potential photocatalyst that has drawn great attention in research and industries in recent years owing to its powerful oxidation capability, nontoxicity, chemical stability, and cost (Samadi et al., 2016). The major advantage of ZnO is that it absorbs a large fraction of the solar spectrum than TiO_2 (Adam et al., 2018; Loh et al., 2018; Varadavenkatesan et al., 2019). To increase the efficiency of ZnO, different methods have been developed. Among these, doping is a widely used technique adopted to improve electrical, optical, and magnetic properties or to modify the structural quality of ZnO nanomaterials (Ebrahimi et al., 2019; A Modwi et al., 2019; Yarahmadi et al., 2021). ZnO nanomaterials have been doped with different metals to decolorize a mixture of dyes in the visible range of the electromagnetic spectrum. Doping ZnO with transition metals such as Co, Mn, Sn, Fe, Cu, and many others to enhance some of its desired features have been practiced (Avadhut et al., 2012; I. Khan et al., 2013; Omri et al., 2013). Application of Ba-doped ZnO nanoparticles in varistors (Fan & Freer, 1997), and liquid sensors (Ando & Miyazaki, 2008), make it a tempting candidate for more uses. The incorporation of Ba into the ZnO matrix has shifted the 371 nm absorption band to 475 nm as observed in photoluminescence spectra for all samples (A Modwi et al., 2019). This red shift in the absorption was reflected in lowering the band energy enabling it to decolorize a dye mixture under visible light illumination.

Besides metal doping, coupling semiconductors has been proven to enhance the charge separation of electron-hole pair which increase the lifetime of the charge carriers and consequently reduce electron-hole recombination (Qin et al., 2017). Graphitic-like carbon nitride (g-C_3N_4) is one of the semiconductor materials with a low bandgap of 2.7 eV which is a potential candidate for coupling with ZnO nanoparticles (Ngullie et al., 2020). g-C_3N_4 turns out to be an intriguing photocatalyst due to its high stability, bulk availability, and low cost (Qi et al., 2020). Among the coupling systems for increasing its photocatalytic efficiency, the ZnO/g-C_3N_4 composite has received significant attention (Ma et al., 2019). The NCs synthesized by coupling ZnO and g-C_3N_4 (ZnO/g-C_3N_4) have far better photocatalytic efficiency than pure ZnO and g-C_3N_4 (Ngullie et al., 2020; Qin et al., 2017). Moreover, the coupling effect not only improved the absorbance band intensity of nanocomposite but also extend the absorption edge to the longer wavelength region (Xing et al., 2015).

ZnO is also a promising antibacterial agent because of its good thermal stability, high antimicrobial activity, and excellent biocompatibility (Svetlichnyi et al., 2016; Zhu et al., 2016). ZnO demonstrates excellent antibacterial activity in a broad spectrum of bacteria, such as *Staphylococcus aureus, Bacillus subtilits, Pseudomonas aeruginosa, Streptococcus pyogenes,* and *Escherichia coli* (Danial et al., 2020; Güy & Özacar, 2016; Lianga et al., 2020; Sohrabnezhad & Seifi, 2016). The interactions between ZnO nanoparticles (NPs) and bacteria are more effective when ZnO particles are reduced to nanoscale size, and bacteria are mostly toxic to die. ZnO NPs are also non-toxic and biocompatible with human cells (Kononenko et al., 2017). With these advantages, ZnO NP can be used as an antibacterial agent. As for photocatalytic activity, it is well established that ZnO impurity doping and coupling can control its properties and may improve its antibacterial activity by increasing the generation of reactive oxygen species (Qamar et al., 2021).

Herein, a new ternary NC (g-C_3N_4/Ba-ZnO) was synthesized via the coprecipitation method for the first time. The synthesized NC was characterized and the results from characterization were well discussed. The photodegradation activity and recyclability of g-C_3N_4/Ba-ZnO for MB degradation under sunlight irradiation were evaluated. Besides, the possible mechanism of MB photocatalytic degradation was proposed. This study demonstrated that the g-C_3N_4/Ba-ZnO photocatalyst is an outstanding alternative for wastewater remediation. Furthermore, the antibacterial activity of this NC was investigated by applying it to gram-positive and gram-negative bacterial strains.

1.2 Statement of the problem

The wastes from the textile and dye industries are highly hazardous to aquatic living and human beings because they cause serious damage to the surrounding environment. The colored organics, especially, induce environmental hazards, and imbalance non-esthetic pollution and eutrophication in the aquatic life. Methylene blue (MB) is one of the extensively used dyes in industries and therefore, it is selected as a model pollutant in this study. It is highly stable with a low degradation capacity and thus, affects the aquatic system. The carcinogenicity, reproductive and developmental toxicity, neurotoxicity, and chronic toxicity towards humans and animals have been experimentally proven (Authority, 2005). It is harmful if swallowed by human beings and animals, and causes irritation to the skin, eyes, and respiratory tract (Rochat et al., 1978). Although there are numerous existing tried and tested methods to accomplish dye removal, most of them have

common disadvantages such as incomplete degradation of pollutants, high energy demand, high cost, and generation of secondary pollution to the environment.

ZnO is a promising candidate due to its remarkable and unique optical and electrical properties. However, the bandgap of 3.37 eV means a large proportion of visible light cannot be utilized efficiently. This study will apply doping and coupling with barium and graphitic carbon nitride respectively, to overcome this limitation. These approaches can not only enhance light utilization efficiency but also inhibit the recombination of charge carriers by forming a heterojunction between individual components.

Bacterial infectious diseases are a serious health problem that has drawn public attention worldwide as a human health threat, which extends to economic and social complications. Due to the excessive use of antibiotics, antibacterial resistance has emerged as one of the greatest threats to human health worldwide. Hence, new strategies and approaches are highly demanded to take the major healthcare challenge posed by rapidly spreading antibiotic-resistant bacteria (Rojas-Andrade et al., 2017). ZnO NPs have proven to be promising antibacterial agents. But ZnO nanostructures' photodynamic antibacterial activity is limited due to the high rate of electron-hole pair recombination and its activation only by UV light. Hence, ZnO nanostructures' antibacterial activity can be effectively enhanced by reducing the electron-hole pair recombination rate. These issues can be resolved by coupling ZnO with another semiconductor which is g-CN and by doping ZnO with barium.

1.3 Objectives

1.3.1 General objective

The general objective of the study was to synthesize barium-doped zinc oxide coupled graphitic carbon nitride nanocomposite (g-C_3N_4/Ba-ZnO) and investigate its photocatalytic and antibacterial activities.

1.3.2 Specific objectives

- To synthesize ZnO, Ba-ZnO, g-C_3N_4, g-C_3N_4/ZnO, and g-C_3N_4/Ba-ZnO nanomaterials
- To characterize the synthesized nanomaterials by using XRD, FTIR, SEM, and UV-DRS.
- To investigate the photocatalytic activity of ZnO NPs, Ba-ZnO NPs, g-C_3N_4, g-C_3N_4/ZnO, and g-C_3N_4/Ba-ZnO NCs by using methylene blue (MB).

- To investigate the antibacterial activity of ZnO NPs, Ba-ZnO NPs, g-C_3N_4, g-C_3N_4/ZnO, and g-C_3N_4/Ba-ZnO against gram-positive and gram-negative bacteria.

1.4 Significance of the study

Industries that release organic dyes are rapidly expanding in developing countries. This industrialization is affecting surface and groundwater. Photocatalysts with large specific surface areas, smaller sizes, and porous structures, which afford good permeability to the dyes for catalytic degradation are being studied worldwide. One of the promising photocatalysts is ZnO NPs, which have a wide band gap energy, large exciton binding energy, enhanced electron mobility, and high catalytic, non-toxic, antimicrobial, and biocompatible features. Moreover, it is reported that the production cost of ZnO NPs is much lower than other nano-photocatalysts. This study applied modifications to ZnO NPs by doping them with barium and coupling them with g-C_3N_4 to overcome problems such as bandgap widening and electron-hole recombination. This study provided information about the antibacterial activity of ZnO NPs, Ba-ZnO NPs, g-C_3N_4, g-C_3N_4/ZnO, and g-C_3N_4/Ba-ZnO NCs by applying them against gram-positive and gram-negative bacterial strains. Furthermore, it can also be used as a basis for further explorations by other researchers.

2. Literature Review

2.1 Dye

Dyes are colorful substances designed to give materials such as fabrics, papers, or any colorable materials a hue. Dyes have been utilized by humans for over a thousand years for various applications. In those days, dyes were usually produced on a small scale from naturally available materials such as insects or plants and are known as natural dyes (Kant, 2012). Synthetic dyes were only recently discovered and their production on large scales started due to the rise in dye demand. An extensive range of synthetic dyes was invented by WH Perkins in the year 1856 spotting various brilliant, colorfast tones for numerous uses (Kant, 2012).

Nowadays, synthetic dyes have become a crucial ingredient widely used to give color to textiles, cosmetics, plastics, and printing (Chaudhary & VIOLET, 2020). This is because dyes are naturally recalcitrant substances and degrading them is not easy or possible. Synthetic dye molecules are complex as well as stable structures due to the presence of auxochromes (water-soluble bonding compounds) and chromophores (color-giving compounds) (Y. Pan et al., 2017). This quality of dyes complicates its degradation process using straightforward methods. The reason why dyes are created this way is so that the color of a dyed material does not fade easily. They are made as complex organic substances so that they can resist getting degraded upon contact with water, detergents, or any other washing agents (Al-Alwani et al., 2018).

2.1.1 Sources of dye pollutants

Synthetic dyes are a necessity in various significant industries such as the leather, paper as well as textile industries for their color-giving properties. It is estimated that 700,000 tonnes of various coloring from about 100,000 commercially accessible dyes are manufactured each year (Abdi et al., 2017; Holkar et al., 2016). Often, once dyes have served their purpose, most of them are discarded without further care into environmental water bodies. Five major industries, shown in Figure 1, are known to be responsible for the presence of dye effluents in the environment. The textile industry (54%) releases the highest amount of dye effluent, contributing to more than half of the existing dye effluents seen in the environment around the world. The dyeing industry (21%), paper and pulp industry (10%), tannery and paint industry (8%), and the dye manufacturing industry (7%) too are known to produce high amounts of dye effluents from various associated processes (De Gisi et al., 2016; Mojsov et al., 2016). The exact amount of dye effluents ejected by

each industry into the environment is unknown but it can be said that the number is quite large to result in a significant environmental issue.

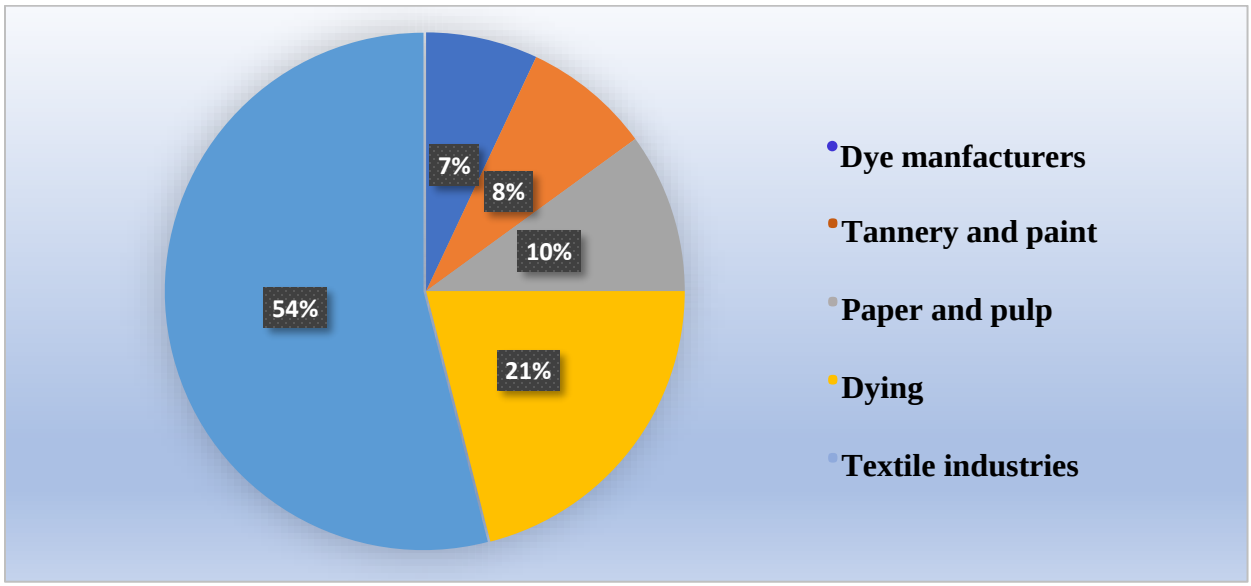

Figure 1: Industries responsible for the presence of dye effluent in the environment (Rauf & Ashraf, 2012).

2.1.2 Dyes in textile industry

Among other dye-utilizing industries, the textile industry is said to utilize the highest amount of dyestuff at approximately 10,000 tonnes per year worldwide (Rodríguez-Couto et al., 2009). Besides that, this industry is also known to produce around 100 tonnes of dye effluent per year, the highest amount of dye wastewater from one industry alone (Solís et al., 2012). High usage of dyestuff in various processes of textile industries results in the generation of huge amounts of dye wastewater. For various processes in the textile industry, specific mixtures of chemicals, dyestuff, and water are prepared. Once the process is complete, the leftover mixture (dye effluent) is discharged into the environment.

2.1.3 Methods of dye removal

2.1.3.1 Conventional dye removal methods

In the late 90s, dye removal methods include only preliminary water purification processes such as equalization and sedimentation since there was no dye effluent discharge limit (Robinson et al., 2001). After permissible dye effluent release standards were established, improvements were made by introducing more effective dye removal methods such as dye-degrading filter beds and activated

sludge processes (Mezohegyi et al., 2012). Following that, a system for dye wastewater treatment shown in Figure 2 was introduced. This system, known as the traditional dye removal method, was implemented by the concerned industries for some time till it was stopped due to its high cost of operation and maintenance (Adegoke & Bello, 2015).

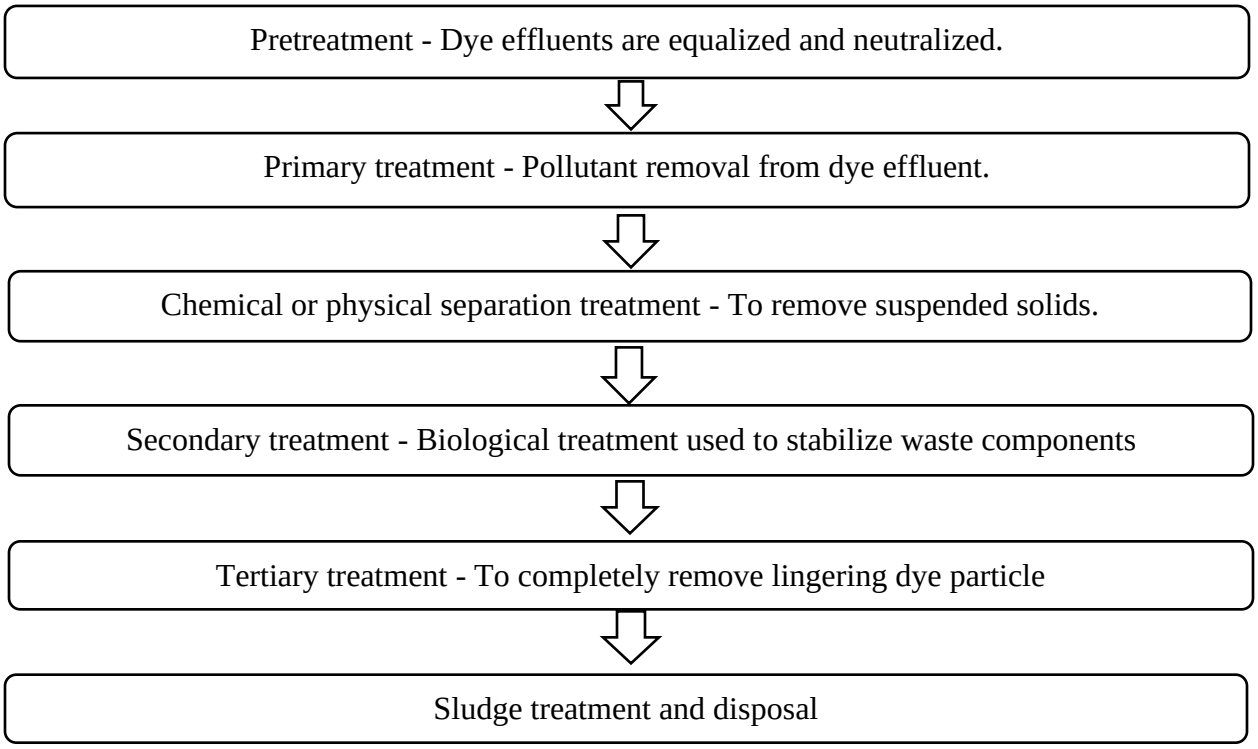

Figure 2: Traditional wastewater treatment system (Katheresan et al., 2018).

Currently, numerous kinds of research are being done to find the ideal dye removal method so that dye wastewater can be recovered and reused (Sarro et al., 2018). Existing methods of dye removal can be separated into three categories namely the biological, chemical, and physical treatments (Tang et al., 2018). Although many dye removal methods have been researched in the past 30 years, only several are truly being implemented by the concerned industries these days because of the limitations posed by the majority of the methods (De Gisi et al., 2016).

2.1.3.2 Biological dye removal methods

In most countries, the typical biological method is the commonly and extensively utilized dye removal method to treat dye wastewater. Generally known as the conventional method, a combination of aerobic and anaerobic processes is carried out before dye effluents are released into the environment (Al-Alwani et al., 2018). This method was chosen as the go-to dye removal

method mainly because it is very cheap and can be accomplished easily (Robinson et al., 2001). As a matter of fact, this treatment alone is insufficient to completely remove hazardous particles from textile dye wastewater which is why colored water is still seen in the environment (Y. Pan et al., 2017). Although the conventional method does treat the chemical oxygen demand present in the wastewater, it does not make the water dye-free or toxic-free. Besides this method, other conventional biological dye removal methods are adsorption by microbial biomass, algae degradation, enzyme degradation, fungal cultures, microbial cultures as well as pure and mixed culture.

Biological dye removal methods incorporate some form of a living organism in its process. This method should be used with caution and engineering ethics should be upheld. The utilization of enzymes to remove dye is becoming quite famous these days as it is believed that branches of biological dye removal methods are the cheapest as well as safest methods of dye removal (Solís et al., 2012). Since this method deals with living things, its major disadvantage is its growth rate. System instability is common in biological dye removal processes as predicting its growth rate and reactions can be tricky at times.

2.1.3.3 Chemical dye removal methods

Chemical dye removal methods are methods utilizing chemistry or its theories in accomplishing dye removal. Conventional chemical dye removal methods are advanced oxidation process, electrochemical destruction, Fenton reaction dye removal, oxidation, ozonation, photochemical and ultraviolet irradiation. Most of the chemical dye removal methods are costly compared to biological and physical dye removal methods with the exception of the electrochemical degradation dye removal method.

Chemical dye removal methods are also commercially unattractive, require specific equipment, and require high electrical energy (Dos Santos et al., 2007). High electrical energy is required to power equipment or reactors in which chemical dye removal takes place. Besides that, chemical, as well as reagent consumption on a large scale, is an issue commonly reported by users of chemical dye removal methods (Crini, 2006). Another undesirable characteristic of this method is the generation of toxic secondary pollution resulting at the end of a chemical dye removal process presenting an additional disposal problem (J. Wang et al., 2018).

2.1.3.4 Physical dye removal methods

Physical dye removal methods are usually straightforward methods commonly accomplished by the mass transfer mechanism. Conventional physical dye removal methods are adsorption, coagulation or flocculation, ion exchange, irradiation, membrane filtration, nanofiltration or ultra-filtration, and reverse osmosis. Among the three methods (biological, chemical, and physical), branches of physical dye removal are the most commonly used methods. These methods are often chosen for their simplicity and efficiency. By far, this method requires the least amount of chemicals compared to the biological or chemical dye removal methods (N. A. Khan et al., 2018). This method does not deal with living organisms and hence is considered to be more predictable than the other two dye removal methods.

2.2 Photocatalysis

The term photocatalysis consists of the combination of photochemistry and catalysis. It implies that light and a catalyst are necessary to bring about or accelerate a chemical transformation. Photocatalysis, using nanosized semiconductor photocatalysts, is a newly emerging clean and cost-effective alternative for a large-scale treatment of water polluted with dyes and other organic compounds (Sanad et al., 2018; Widiyandari et al., 2018). The advantages of using metal-oxide semiconductors, such as titania (TiO_2) and zinc oxide (ZnO), are not only their high photocatalytic efficiency but also their high photosensitivity, non-toxic nature, low cost, and eco-friendliness. But, the above photocatalysts have their limitations; in that, these have a high band gap (>3.0 eV), therefore can only be photoexcited in the ultra-violet (UV) region of electromagnetic radiation. As the UV component of solar radiation, reaching the Earth's surface is merely 4 to 5 % of the solar spectrum, therefore, the photocatalytic efficiency of the above photocatalysts is low under sunlight.

2.2.1 Semiconductor photocatalysis mechanism

In an ideal photocatalytic process, organic pollutants are mineralized into carbon dioxide (CO_2), water (H_2O), and mineral acids in the presence of ZnO particles and reactive oxidizing species, such as oxygen or air. The photocatalytic reactions were initiated when the ZnO particle absorbs photons with energies greater than that of its band gap energy from the illumination. In this way, the photo-induced electron is promoted from the valence band (VB) to the conduction band (CB), forming a positive hole (h_{VB}^{+}) and electron (e_{CB}^{-}) on the surface of ZnO particle (Equation 1).

$$ZnO + h\nu \rightarrow ZnO\ (e_{CB}^{-} + h_{VB}^{+}) \quad (1)$$

$$e_{CB}^{-} + h_{VB}^{+} \rightarrow heat \quad (2)$$

$$e_{CB}^{-} + O_2 \rightarrow \bullet O_2^{-} \quad (3)$$

$$h_{VB}^{+} + OH^{-} \rightarrow \bullet OH \quad (4)$$

$$\bullet OH + R\text{-}H \rightarrow R'\bullet + H_2O \quad (5)$$

$$h_{VB}^{+} + R \rightarrow R^{+}\bullet \rightarrow \text{Intermediates} \quad (6)$$

$$e_{CB}^{-} + O_2 \rightarrow \bullet O_2^{-} + H^{+} \rightarrow HOO\bullet + \bullet O_2^{-} \rightarrow HOO\bullet + O^{-} \quad (7)$$

$$HOO\bullet \rightarrow H_2O_2 + O_2 \quad (8)$$

$$H_2O_2 + \bullet O_2^{-} \rightarrow \bullet OH + OH^{-} + O_2 \quad (9)$$

It should be noted the photo-generated holes in the valence band will recombine with the photo-excited electrons in the conduction band and dissipates in the form of heat (Equation 2). Therefore, the presence of oxygen as electron scavengers prolongs the recombination of electron-hole pairs while forming the superoxide radicals ($\bullet O_2^{-}$) (Equation 3). The reaction of h_{VB}^{+} with OH^{-} (Equation 4) may lead to the formation of hydroxyl radicals. The hydroxyl radical is an extremely strong, non-selective oxidant (E_0 = +3.06 V) which leads to the partial or complete mineralization of organics (Equation 5). Moreover, the high oxidative potential of the hole in the photocatalyst also permits the direct oxidation of organic matter to reactive intermediates as shown in Equation 6. The superoxide radicals were further protonated to produce hydroperoxyl radical (HOO•) and subsequently H_2O_2 (Equations 7-9). The HOO• also functions as an electron scavenger to trap conduction band electrons which further delays the recombination process. The general photocatalysis mechanism processes are shown in Figure 3.

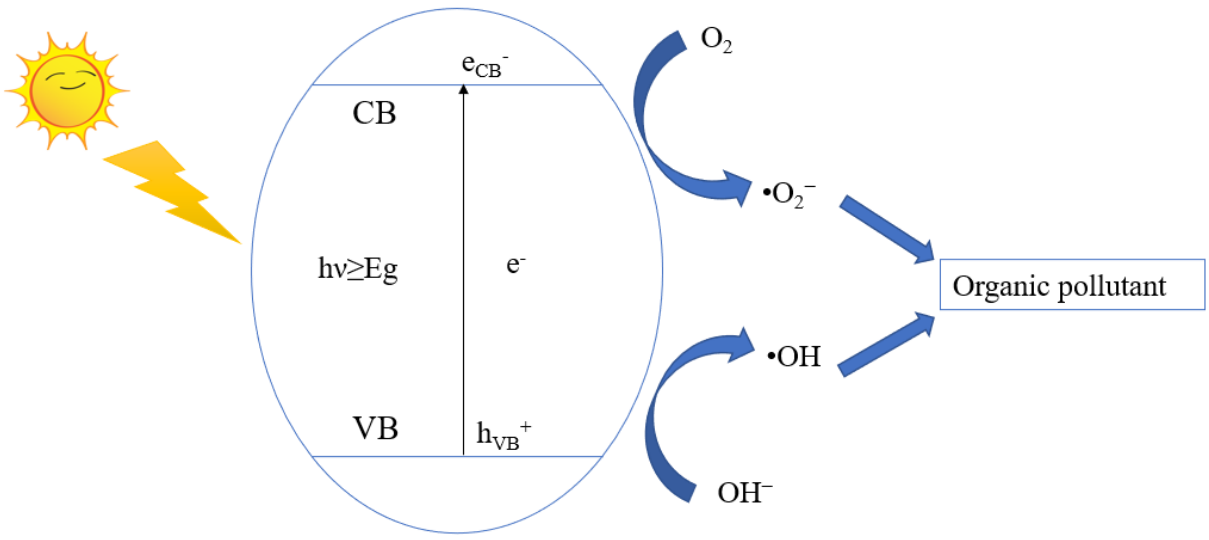

Figure 3: General mechanism of photocatalysis.

2.1.2 Factors affecting photocatalysis

The oxidation rates and efficiency of the photocatalytic system are highly dependent on a number of operational parameters that govern the photodegradation of the organic molecule. Several studies have reported the significance of operational parameters. The photodegradation of organic pollutants depends on some basic parameters which are the amount of pollutant, amount of photocatalyst, pH of the solution, the temperature of a reaction medium, time of irradiation of light, the intensity of light, size, morphology, and surface area of photocatalyst, nature of the photocatalyst, nature of the substrate, and structure of photocatalyst and substrate. The photodegradation of organic compounds has been studied by several scientists and concluded the optimum conditions for the photodegradation of organic compounds.

2.1.2.1 Amount of Catalyst

Generally, the amount of photodegradation of water pollutants increases with an increase in the amount of catalyst dosage. This is due to the exposure of more active sites on the photocatalyst, which adsorb more photons and produces more OH• radicals and positive holes under irradiation. These hydroxyl radicals and positive holes take participation in the photocatalytic reaction, and thus, the rate of degradation of pollutants increases. At a lower dosage of catalyst, most of the irradiated solar light is directly transmitted from the solution, and a little part of it was consumed by the catalyst to perform. However, a higher dosage of catalyst, beyond a certain limit, decreases

the rate of photo-degradation of pollutants. One of the possible reasons might be the turbidity of the solution, which increased with the amount of catalyst and blocks the UV/Vis radiation inside the solution and also enhances the light scattering. This results in a less number of photoactive species and consequently the percentage of degradation also reduces. Another reason might be the agglomeration of nanoparticles at high concentrations in the solution, which reduces the number of active surface sites available for exposure (Sohrabnezhad et al., 2009).

2.1.2.2 Amount of pollutant

Photocatalysis depends on the adsorption of pollutants on the surface of the photocatalyst. In the photocatalysis process, only the amount of organic pollutant adsorbed on the surface of the photocatalyst contributes and not the one in the bulk of the solution. The adsorption of organic molecules such as dyes depends on the initial concentration of the dye. The initial concentration of dye in a given photocatalytic reaction is an important factor that needs to be taken into account. In General, the percentage degradation decreases with an increasing amount of dye concentration, and with a constant photocatalyst amount. Boruah and coworkers studied the effect of initial dye (MG, MB, and RhB) concentration on photodegradation (Boruah et al., 2016). The degradation efficiencies of the selected model dye molecules were investigated by varying the concentration of dye molecules from 0.08 mM to 0.5 mM at a fixed concentration of the photocatalyst of 0.5 g L^{-1} at pH 5. It was observed that the degradation efficiency decreased with increasing dye concentration due to the unavailability of active sites on the photocatalyst. Figure 4 shows the dye degradation efficiency of MG, MB, and RhB dye molecules with more than 98% when the initial concentration dye is 0.1 mM. However, the degradation is found to decrease as the initial concentration of the dye molecules increases. Moreover, due to the dimerization effect of RhB at higher concentrations, only 87.13% degradation efficiency was achieved at pH 5.

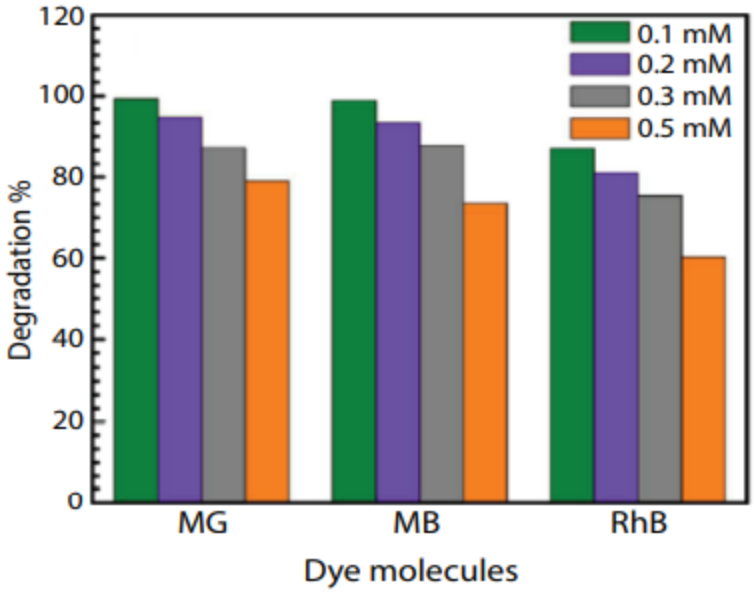

Figure 4: Photodegradation efficiency of MG, MB, and RhB dye molecules at different initial concentrations of MG, MB, and RhB (Boruah et al., 2016).

2.1.2.3 Effect of pH

The Photodegradation of organic pollutants is affected by the pH of the solution. However, the interpretation of pH effects on the efficiency of the photodegradation process is a difficult task. This is because three possible reaction mechanisms can contribute to dye degradation, (1) hydroxyl radical attack, (2) direct oxidation by the positive hole, and (3) direct reduction by the electron in the conducting band. The contribution of each one depends on the substrate's nature and pH (Samsudin et al., 2015).

The variation of solution pH changes the surface charge of photocatalysts and shifts the potentials of catalytic reactions. As a result, the adsorption of pollutants on the surface is altered thereby causing a change in the reaction rate. The pH of the solution influences the surface charge, degree of ionization, agglomeration, oxidation potential of the valence band of the photocatalyst, and the adsorption of the pollutant (N. Kumar et al., 2018). With an increase in the pH value, • OH is easily generated by the reaction between positive hole sand hydroxyl ions; thus, the efficiency for the degradation is also enhanced. However, photo-degradation efficiency generally decreased at too high pH (pH > 11), as the production of excess hydroxyl ions starts the competition with pollutants to get adsorb onto the surface of the catalyst and/or neutralized the acidic sites on the photocatalyst

(Rajabi et al., 2013). Conversely, the low pH of the medium is beneficial for the photodegradation of anionic species (Karunakaran & Dhanalakshmi, 2008). However, at low pH, due to the protonation of the photocatalyst surface, the adsorption of cationic pollutants reduces, which went up directly to the decline in photodegradation. Also, at too low pH anionic pollutants start protonation, which avoids the adsorption on the positive surface of the photocatalyst, necessary for the photocatalytic reaction through electrostatic repulsion. The unavailability of hydroxyl ions at low pH, required for the photocatalytic reaction suppressed the degradation of water pollutants. Thus, based on pollutants and zero-point charge (pHpzc) of photocatalyst, optimization of pH is one of the necessitated steps. For example, photo-degradation of malachite green is favored at a low pH medium, while methylene blue efficiently degrades at a high pH medium using the TiO_2-based photocatalyst (Prado & Costa, 2009). Boruah and colleagues studied the degradation of three dye molecules in the pH range of 3 to 11 at a fixed catalyst concentration and dye concentration (Fig. 5) (Boruah et al., 2016). It was observed that maximum degradation efficiency appeared at pH 11 for MG (100%) and RhB (94.7%) i.e., degradation efficiency increased with increasing pH. However, in the case of MB anionic dye molecule, the rate of degradation increases up to pH 5 and then decreases. The maximum degradation of the MB is 98.97%, achieved at pH 5 under same experimental conditions.

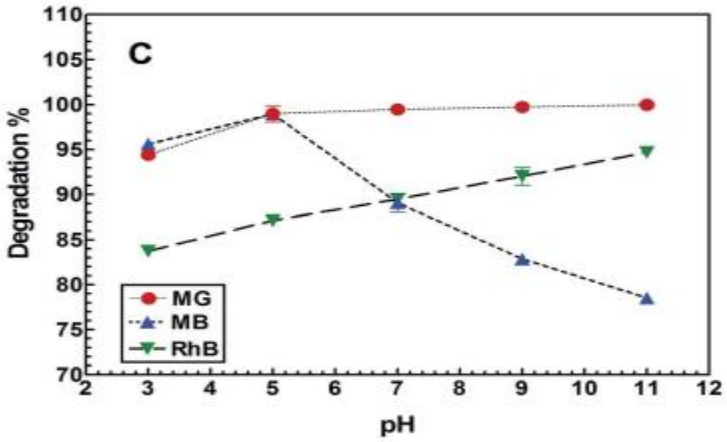

Figure 5: Effect of varying initial pH on Photodegradation efficiency of MG, MB, and RhB dye molecules (Boruah et al., 2016).

2.1.2.4 Effect of Size, Morphology, and Surface Area

Surface morphology such as particle size and agglomerate size is an important factor to be considered in the photocatalytic degradation process because there is a direct relationship between organic compounds and the surface coverage of the photocatalyst (Abbas & Bidin, 2017). Generally, small-size nanoparticles exhibit greater surface area and produce a number of active sites which takes participation in the direct adsorption of contaminant onto the surface or adsorb the photons efficiently and leads to better mineralization (N. Kumar & Ray, 2018). Figure 6 shows the photodegradation of rhodamine B dye with pure ZnO and Cu-ZnO nanocomposites. The maximum photodegradation is found in the case of Cu-modified ZnO and whereas in the case of ZnO, less photodegradation occurs (Karthik et al., 2022). This is because the surface of ZnO is different from the surface of Cu-doped ZnO.

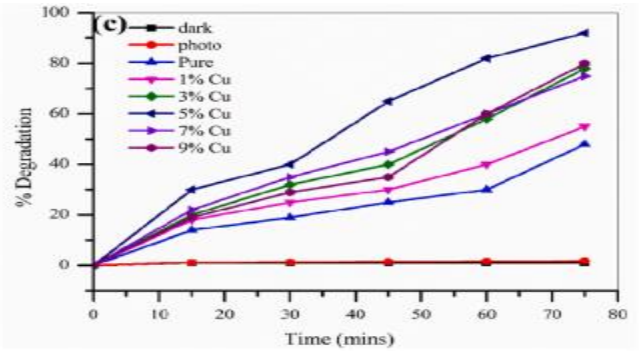

Figure 6: Degradation efficiency of RhB by ZnO and Cu-ZnO under UV-light irradiation (Karthik et al., 2022).

The morphology of nanomaterials can control the efficiency of photocatalysts toward the degradation of contaminants. For instance, Kumar et al. tested the various ZnO morphologies (nanorod, nanoflower, and nanospindle) for the photodegradation of anionic dye MO. The results highlight that rod-like structures have higher catalytic activity than flowers and spindle structures due to the formation of high amounts of reactive species along the longitudinal surface of ZnO nanorods (N. Kumar et al., 2015).

In another similar work two different synthesized ZnO nanostructures with flower-like and spherical morphologies (Kajbafvala et al., 2012). The results depict that the efficiency of photocatalytic performance in the Zinc oxide nanostructures with spherical morphology is greater than that found in the flower-like Zinc oxide nanostructures as well as bulk ZnO.

2.1.2.5 Effect of light intensity

Semiconductor material which acts as a photocatalyst in the photocatalytic reaction absorbs the light to initiate the reaction. The energy of the light should be equal to or more than the bandgap of the photocatalyst to excite the electron of the valence band to jump in the conduction band and leaves the positive holes behind in the valence band (Sohrabnezhad et al., 2009). It has been shown that at low light intensities (0-20mW/cm^2), the rate would increase linearly with increasing light intensity (first order), whereas at intermediate light intensities (25mW/cm^2) the rate would depend on the square root of the light intensity (Asahi et al., 2001). At high light intensities, the rate is independent of light intensity, because at low light intensity reactions involving electron-hole formation are predominant and electron-hole recombination is negligible. On the other hand, when light intensity is increased, the electron–hole pair separation competes with recombination, thereby causing lower effect on the reaction rate.

2.1.2.6 Effect of temperature

Generally, photocatalytic reactions are conducted at room temperature. However, due to the release of energy during the degradation reaction and recombination of electron and hole pairs, the temperature of the reaction increases. On increasing the temperature of the reaction, the rate of photocatalytic degradation also increases steadily. However, if the reaction temperature >80°C promotes the recombination of charge carriers and disfavors the adsorption of organic compounds on the Titania surface (Hashimoto et al., 2005). A reaction temperature below 80°C favors the adsorption whereas further reduction of reaction temperature to 0°C results in an increase in the apparent activation energy. Therefore, a temperature range between 20-80°C has been regarded as the desired temperature for effective photo mineralization of organic content (Mamba et al., 2014).

2.3 ZnO as a photocatalyst

ZnO is a representative n-type semiconductor, with a wide band gap of 3.37 eV and a high excitation binding energy of 60 meV, and produces electron-hole pairs under UV light or visible light irradiation (Vinitha et al., 2021). The electron and hole can interact with the O_2 adsorbed on the surface of the photocatalyst and H_2O to generate $\cdot O_2^-$ and ·OH, respectively, which can reduce and oxidize the organic contaminants completely into their respective end products (CO_2 and H_2O, respectively) (M. M. Khan et al., 2014; Senapati et al., 2012). ZnO nanoparticles are synthesized

through various techniques, such as co-precipitation (Lang et al., 2016), microwave (V. Kumar et al., 2016), hydrothermal (Kumaresan et al., 2017), and sol-gel method (Hasnidawani et al., 2016).

In recent studies, special attention has been given to zinc oxide (ZnO) nanoparticles (NPs) as semiconductor catalysts with important properties, such as high chemical stability, nontoxicity, great optical and electrical properties, and high oxidizing potential (Loh et al., 2018). These NPs have been used for the decomposition and oxidation of resistant organic pollutants. ZnO nanostructures with different morphologies and properties have attracted much attention for photocatalytic applications, in both environment and energy fields. Up to now, a lot of papers have been published on the photocatalytic performance of ZnO nanostructures. For example, Morteza G. and coworkers synthesized ZnO NPs using a green method (Golmohammadi et al., 2020). ZnO NPs exhibited a great photocatalytic performance, which resulted in degradation efficiencies of about 92% and 86% within 5 h at the rate constants of 8.7 $\times$10 - 3 min^{-1} and 6.7 $\times 10^{-3}$ min^{-1} for MB and ECBT, respectively. Similarly, Vanna and coworkers studied photocatalytic degradation of MO under solar irradiation by ZnO nanoparticles fabricated by a simple and low cost precipitation method (Sanna et al., 2016). The ZnO nanoparticles showed excellent photodegradation efficiency and good recycling performance, supporting the potential application as economical and highly sunlight-active material to treat wastewater containing azo dyes. In another study, the synthesis of Ag-doped ZnO NPs by co-precipitation method is reported (R. Singh et al., 2017). The Ag/ZnO NPs with different weight percentage of Ag relative to ZnO were applied under visible light irradiation for evaluating heterogeneous photocatalytic degradation of methylene blue (MB) and brilliant blue (BB) respectively. The presence of Ag in ZnO enhances MB and BB dye degradation effectiveness from 96.78 to 98.66 and 82.15 to 97.36% for pure ZnO and maximum Ag doped ZnO respectively.

2.3.1 Improvement of ZnO as photocatalyst

photocatalytic reactions are mainly governed by bandgap energy and hydroxyl radicals. The main drawback for ZnO semiconductors as photocatalysts is their large band gap energy, which is active only under UV light irradiation but is not active to absorb visible light; as a result, the efficiency of utilizing sunlight is limited (Aponiene & Luksiene, 2015). Doping has thus been adopted to modify the physical and chemical properties of ZnO by incorporating impurities such as metals or non-metals, to shift the valence band energy of ZnO upward and narrow the bandgap energy to the

ultraviolet-visible region (Z. Yu et al., 2013). Metal doping could counter the recombination problem by enhancing the charge separation between electrons and holes. In addition, the dopants may trap electrons, reducing the chances of electron-hole recombination that deactivates the photocatalytic system (Sanchez & Lopez, 1995). Furthermore, the generation of hydroxyl radicals and active oxygen species will greatly increase resulting from enhancement in charge separation efficiency. Generally, the concentration and ion nature of the dopant, synthesis method, and operating conditions significantly affect the photoactivity of the metal-doped semiconductor. Alternatively, the coupling of semiconductors having different band gap have also leads to improve their photocatalytic performance (Ngullie et al., 2020).

2.3.1.1 Doping

In recent years, efforts have been made to modify the high bandgap photocatalysts by doping with metals and non-metals to enhance their photocatalytic performance (I. Khan et al., 2013; Omri et al., 2013).

Generally, photocatalytic reactions under visible light require band gap narrowing of ZnO. Bandgap narrowing through ZnO doping can be achieved by three main approaches, i) the elevation of the valence band maximum, ii) the lowering of the conduction band minimum, and iii) the introduction of localized energy levels within the band gap (Coronado et al., 2013). Figure 7 illustrates the three different situations for achieving visible-light-driven photocatalysts such as ZnO by metal and nonmetal doping.

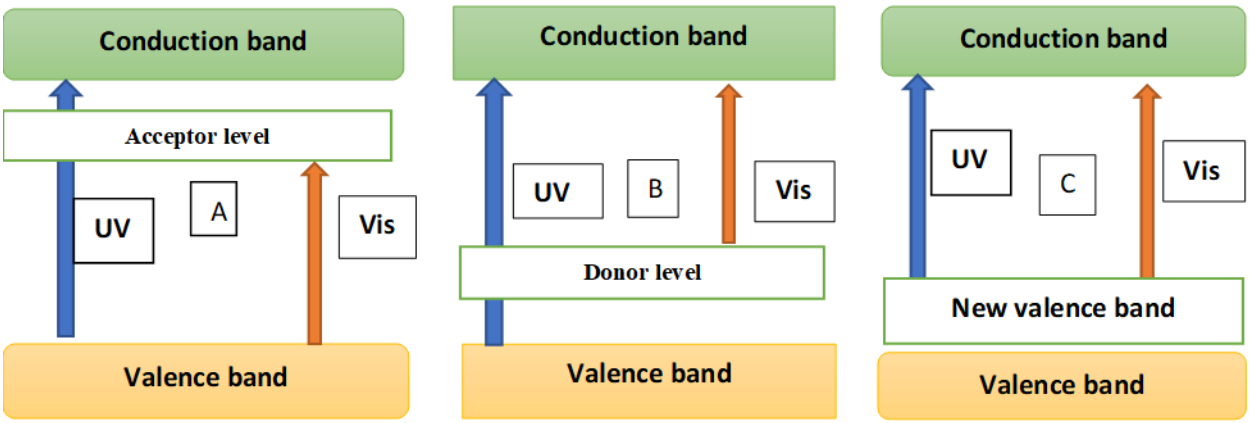

Figure 7: Schematic representation of the doped ZnO energy levels: (a) acceptor level and (b) donor level with metal doping, (c) new valence band formation by nonmetal doping (Chen et al., 2010).

2.3.1.1.1 Metal doping

Metal doping has been proven to shift the absorption edge of the semiconductor photocatalyst to the visible range using less than 10 at% of foreign cations (Coronado et al., 2013). The interaction of the metal cation states with the valence or conduction band of ZnO leads to the creation of intra-band gap levels and induces band gap narrowing. Fig. 8(a) shows p-type doping with metal ions as electron acceptors, which introduces a level below the original conduction band in the band gap. In addition, n-type doping of metal ions as an electron donor creates a level above the valence (see Fig. 7(b)). These new states can absorb light with longer wavelengths. Depending on the electronegativity, ionic radius, and concentration, the metal dopants occupy substitutional or interstitial sites in the ZnO lattice or segregate to grain boundaries. Although the mid-gap level states created by metal doping extend the light absorption to the visible-light range, they may deteriorate the photocatalytic activity because the new states can act as charge recombination centers (Chen et al., 2010).

Some properties of ZnO are important for its practical applications in various fields. The preparation of new photocatalysts by incorporation of other elements is an important challenge in the development of ZnO photocatalysts. Although ZnO is a good photocatalyst, the doped ZnO surpasses its photocatalytic efficiency. Modification of ZnO by cationic dopants is currently another important technology being used by many researchers. The doped ZnO possesses a prominent photodegradation performance than the undoped ZnO. Moreover, the structural, optical, chemical, electrical, and magnetic properties of ZnO can be tuned by the addition of a selected cationic dopant. The ZnO has been doped with elements such as Cu (Sajjad et al., 2018), Ni (Devi et al., 2021), Co (H. Pan et al., 2020), Mn (Chanu et al., 2019), and Al (Mahdavi & Talesh, 2017). The cationic doping is performed essentially by the addition of transition metals, group I, and group V elements. The incorporated elements are usually isomorphic to zinc ions, such as Cu^{2+}, Ni^{2+}, $Co^{2+,}$ and Mn^{2+}. The effect of a modified photocatalyst can be characterized by the photodegradation of a selected organic pollutant. In recent years, many photocatalytic studies reveal that the cationic dopant strongly improved the photocatalytic activity of ZnO. The results indicated that the cationic-doped ZnO has better photocatalytic activity than the undoped ZnO. The doped ZnO exhibits faster response to the photodegradation of many organic pollutants. The influence of various metal dopants in the photocatalytic property of ZnO is summarized in Table

1. Comparison of the photodegradation in various organic pollutants is studied on both undoped and metal-doped ZnO.

Table 1: Influence of metal dopant on photocatalytic activity of ZnO.

Dopant	Experimental condition			Efficiency (%)		References
	Light source	dye	Irradiation time	ZnO	Doped ZnO	
Sn	UV light	Methyl orange	300 min	85.4	98.8	(Beura et al., 2018)
Cu	Visible light	Malachite green	60 min	15	99.25	(Adsorption Modwi et al., 2017)
Ag	Sunlight	Methyl violet	180 min	45	95	(Ashebir et al., 2018)
Mn	Sunlight	Malachite green	120 min	57.5	94.4	(Mohamed & Shawky, 2018)
Ni	halogen lamp	Methyl green	240 min	25	~100	(Abdel-Wahab et al., 2016)
Fe	mercury bulb	Methyl orange	140 min	88	94	(Isai & Shrivatava, 2019)
Sr	Metal halide lamp	Methylene blue	120 min	56.0	97.0	(Yarahmadi et al., 2021)
Mg	Hg arc lamp	Rhodamine B	120 min	13.18	78.02	(Sadaiyandi et al., 2018)
Eu	UV Philips lamp	Eriochrome black T	240 min	80	~100	(Franco et al., 2020)
La	mercury vapor lamp	Rhodamine B	120 min	~70	~95	(M. Kumar et al., 2021)

2.3.1.1.2 Nonmetal doping

Nonmetal doping of ZnO, which is expected to substitute oxygen atoms, has been intensively investigated. In this regard, different photocatalysts with promising results under visible light have been obtained. As discussed above, the hybridization of nonmetal dopant orbitals and O 2p states of ZnO raise the upper edge of the valence band and thus narrow the band gap. Elements with lower electronegativity than oxygen and similar size to that of lattice O atoms are two main requirements for effective nonmetal dopants (Coronado et al., 2013). ZnO doping with nonmetals, such as carbon (C), nitrogen (N), and sulfur (S) can lead to the formation of intermediate energy levels and extend the valence band, which causes visible-light photocatalytic activity (Kadam et al., 2014).

Table 2: Influence of nonmetal dopant on photocatalytic activity of ZnO.

Dopant	Experimental condition			Efficiency (%)		Reference
	Light source	dye	Irradiation time	ZnO	Doped ZnO	
C	Sunlight	Rhodamine B	30 min	40.0	100	(Haibo et al., 2013)
C	Xe lamp	Rhodamine B	120 min	26.0	98.0	(Y. Wang et al., 2020)
N	Xe lamp	Methyl orange	100 min	20.0	100	(Sun et al., 2013)
N	Xe lamp	Rhodamine B	90 min	90.46	100	(Dindar & Güler, 2018)
S	Sunlight	Resorcinol	420 min	~ 55.0	100	(Patil et al., 2010)
S	Halogen lamp	Rhodamine B	90 min	-	100	(Mirzaeifard et al., 2020)

2.3.1.2 Constructing heterojunctions

Among the coupling systems for increasing ZnO's photocatalytic efficiency, the ZnO/g-C_3N_4 (zinc oxide/graphitic carbon nitride) composite has received significant attention because of varying interfacial interactions provide new properties, which do not belong to any individual nanomaterial (K. Q. B. C. J. Yu & Ho, 2017). The ZnO/g-C_3N_4 composite has far better photocatalytic efficiency than pure ZnO and g-C_3N_4 (Uma et al., 2017). This coupling effect improved the absorbance band intensity of the composite and also extended the absorption edge to the longer wavelength region.

2.3.1.2.1 Graphitic Carbon Nitride

The large band gap energy of semiconductor photocatalysts, such as the traditional TiO_2 and ZnO, remains the bottleneck to satisfy the requirements of visible light applications, due to the low utilization of solar energy (Tan et al., 2016). Therefore, in the search for robust and visible light-active semiconductor photocatalysts, a polymeric semiconductor, namely graphitic carbon nitride (g-C_3N_4), has elicited ripples of excitement in the research communities as the next-generation photocatalyst. Graphitic carbon nitride (g-C_3N_4) is a two-dimensional conjugated polymer consisting of carbon and nitrogen. It is obtained from different carbon materials analogues by replacing carbon atoms with nitrogen atoms (Magesa et al., 2019). Due to its facile synthesis, appealing electronic band structure, high physicochemical stability, and earth-abundant nature, it is considered a promising photocatalyst (Qin et al., 2017).

In comparison with TiO_2 and ZnO, g-C_3N_4 has a moderate band gap of 2.7−2.8 eV, resulting in an onset visible light absorption of around 450−460 nm (Dong et al., 2013). As the most stable allotrope in all C_3N_4 structures, g-C_3N_4 is thermally stable up to ca. 600 °C in air, as evidenced by thermogravimetric analysis, which can be ascribed to the aromatic C−N heterocycles (Fang et al., 2011; X. Wang et al., 2012). In addition to that, g-C_3N_4 is also chemically stable and not dissolved in acid, alkali, or organic solvents, rendering it a robust material under ambient conditions (Martin et al., 2014).

As a matter of fact, copolymerization and doping are effective approaches to introduce impurities into the g-C_3N_4 matrix to modify the electronic structure and energy band configuration (X. Li et al., 2016; Ngullie et al., 2020; Qin et al., 2017). The development of modified g-C_3N_4-based heterojunction photocatalysts with improved physicochemical properties for remarkable

photocatalytic activity is an increasing requirement to advance g-C_3N_4 for target-specific applications. To date, researchers have attempted to enhance the photocatalytic performance of g-C_3N_4 via noble metal deposition (G. Zhang et al., 2016), metal doping (Z. Li et al., 2016), the incorporation with carbonaceous nanomaterials (Zhou et al., 2016), the coupling with other semiconductors (Lu et al., 2016), and many others. Recently, g-C_3N_4 as a promising candidate widely used to couple with other semiconductors to form hetero-structured photocatalysts with enhanced photocatalytic performance because of their similarity to graphene. For example, g-C_3N_4/TiO_2 (Lu et al., 2016), g-C_3N_4/ZnO (Ngullie et al., 2020), g-C_3N_4/Bi_2WO_6 (Y. Wang et al., 2018), g-C_3N_4/$SrTiO_3$ (Luo et al., 2019), g-C_3N_4/BiOBr (Shi et al., 2020), g-C_3N_4/WO_3 (W. Yu et al., 2017), and g-C_3N_4/Ag_3PO_4 (Raeisi-Kheirabadi & Nezamzadeh-Ejhieh, 2020) were prepared and used for the photodegradation of organic pollutants.

Concerning the typical inorganic semiconductor photocatalysts (e.g., TiO_2, ZnO), g-C_3N_4 also suffers several intrinsic drawbacks such as high recombination rate of charge carriers, low electrical conductivity, and the lack of absorption above 460 nm. To synthesize highly efficient g-C_3N_4-based nanostructures, several important criteria must be fulfilled: (1) accelerating the charge transfer and separation to inhibit the recombination rate, (2) enhanced exposure of solar light absorption, and (3) high photochemical stability of the catalysts for a prolonged duration. Generally, hybrid nanocomposites offer various promising merits: (1) the visible light utilization is improved, (2) the presence of cocatalysts lowers the redox overpotential at the active sites, (3) charge transfer and separation through the Schottky junction (metal/semiconductor heterostructures) or a p-n junction (semiconductor/semiconductor heterostructures) is expedited, and (4) the system stability by protecting the active sites and functional groups on the surface of the semiconductor through proper surface passivation is ameliorated. In this context, the formation of heterojunction nanocomposites has become a compelling and feasible approach to overcome the above issues to advance g-C_3N_4 in terms of photocatalytic activity. Due to the flexibility of g-C_3N_4 nanosheets as well as their opened-up 2D flat morphology, this favors g-C_3N_4 nanosheets to act as an ideal platform for the formation of heterojunctions with various components.

2.3.1.2.2 Metal oxides/g-C_3N_4 Hybrid Heterostructures

The development of a semiconductor heterojunction by incorporating two different catalysts with appropriate VB and CB potentials is regarded as one of the effective techniques for promoting charge transfer and separation by taking into account the space charge depletion and accumulation between two semiconductors. Until now, many research groups have developed different types of g-C_3N_4-based semiconductor heterojunctions for applications in environmental remediation and solar energy conversion (Christoforidis et al., 2016). Among various metal oxides, ZnO is a widely reported type of metal oxide which can be hybridized with g-C_3N_4. For example, J. Qin et al reported the synthesis of 2D sheet-like carbon-doped ZnO/g-C_3N_4 nanocomposites. The obtained sheet-like carbon-doped ZnO/g-C_3N_4 nanocomposites exhibited enhanced photodegradation efficiency under visible light irradiation for MB than pure ZnO, g-C_3N_4, and pure TiO_2. The better degradation efficiency was achieved when the content of g-C_3N_4 is 23.5 wt% and 43 wt% and the apparent rate constant of carbon-doped ZnO/g-C_3N_4 is approximately 4 times, 4 times, and 13 times higher than those of pure ZnO, g-C_3N_4, pure TiO_2, respectively (Qin et al., 2017). In another study, ZnO/g-CN nanostructured composites were fabricated by adding different amounts (60, 65, 70, and 75 wt.%) of g-CN into ZnO via the simple hydrothermal process (Ngullie et al., 2020). Among fabricated composites, the 75% ZnO/g-CN nanocomposites displayed a superior PCA for MB degradation, which was a three-fold enhancement over the pure ZnO nanoparticles (Ngullie et al., 2020). Zhang and coworkers also reported that a series of g-C_3N_4/ZnO nanocomposites prepared through two distinct procedures of a low-cost, environmentally-friendly, in-situ fabrication process, with urea and zinc acetate being the only precursor materials (S. Zhang et al., 2019). These nanocomposites' photocatalytic properties were evaluated by MB dye photodegradation under UV and sunlight irradiation. Interestingly, compared with ZnO nanorods, g-C_3N_4/ZnO nanocomposites showed enhanced photocatalytic activity that can be ascribed to the effective establishment of heterojunctions. In another recent study, A unique nanocomposite consisting of 60% g-C_3N_4 hybridized with 7% Cd-ZnO (60% g-C_3N_4/Cd-ZnO) was synthesized using a simple co-precipitation method by Sher et al. (Sher, Javed, Shahid, et al., 2021a). Its enhanced photocatalytic and antibacterial activity was attributed to the formation of a well-defined heterojunction between the g-C_3N_4 nanosheets, and rod-like Cd-doped ZnO NPs, which were verified by the characterization results. Ternary NCs, in which 60% g-C_3N_4 hybridized with 7% Cd-doped ZnO (g-C_3N_4/Cd-ZnO) NCs were proven to be optimum visible-light-driven (VLD)

photocatalysts for the degradation of MB dye. The enhanced photodegradation of MB is mainly due to the increase in the generation of photogenerated charge carriers.

Table 3: Comparison of photocatalytic efficiency of previously studied g-C_3N_4/ZnO NCs.

photocatalyst	Light source	pollutant	Irradiation time	Efficiency (%)	References
g-C_3N_4/ZnO	Visible light	Rhodamine B	100	97.4	(Liu et al., 2012)
g-C_3N_4/ZnO	Sunlight	Cephalexin	60	98.9	(Li et al., 2018)
g-C_3N_4/ZnO	UV light	Direct blue 199	100	99	(Sundaram et al., 2017)
g-C_3N_4/ZnO	Visible light	Rhodamine B	90	98.5	(Zhong et al., 2020)
g-C_3N_4/ZnO	UV light	Methylene blue	180	98	(Ngullie et al., 2020)
g-C_3N_4/ZnO	Visible light	Methylene blue	90	73	(Hakimi-Tehrani et al., 2021)

3. Materials and Methods

3.1 Reagents

The materials used for the synthesis of Ba-ZnO/g-C_3N_4 nanocomposites were zinc acetate dihydrate ($Zn(CH_3COO)_2 \cdot 2H_2O$), barium chloride dihydrate ($BaCl_2 \cdot 2H_2O$), urea, sodium hydroxide (NaOH), ethanol, and distilled water. All chemicals and reagents were purchased from Rhanchem chemicals with analytical grade and used as received without further purification.

3.2 Synthesis of ZnO NPs

Pure ZnO NPs were prepared by using a co-precipitation method. First, 0.1 M of zinc acetate dihydrate was prepared. 100 mL of the prepared zinc acetate solution was then added to a 250 mL beaker. After 30 min of stirring, 60 mL of NaOH (2 M) solution was added dropwise to the zinc acetate solution. Then, the solution was further stirred for 1 h and it was allowed to settle. After that, The prepared NPs were separated through decantation and washed three times using distilled water and ethanol. Finally, ZnO NPs in the form of powder was obtained by drying the product using an oven at 100 ^oC for 8 h (A Modwi et al., 2019).

3.3 Synthesis of Ba-ZnO NPs

For the preparation of Ba-doped ZnO NPs, zinc acetate dihydrate ($Zn(CH_3COO)_2 \cdot 2H_2O$) and barium chloride dihydrate ($BaCl_2 \cdot 2H_2O$) were used as precursor materials. Firstly, 0.1 M of zinc acetate dihydrate and 0.05 M, 0.1 M, and 0.15 M of barium chloride dihydrate solutions were prepared. In a typical method, 100 ml of 0.1 M zinc acetate dihydrate solution was placed into three different 250 ml beakers under stirring conditions. Next, 40 ml aqueous solution of barium chloride dihydrate with concentrations of 0.05 M, 0.1 M, and 0.15 M was added slowly under vigorous stirring to the three zinc acetate solutions. After 30 min, 60 ml of NaOH (2 M) was added dropwise to the mixture of starting materials. Afterwards, the solution was stirred for 1 h after the addition of NaOH. The prepared NPs were separated through decantation and the precipitates were washed three times with distilled water and ethanol. After washing, the precipitates were recovered and dried at 100 ^oC in an oven for 8 h (A Modwi et al., 2019).

3.4 Synthesis of g-C_3N_4

The g-C_3N_4 was fabricated via a facile thermal condensation method in which 10 g of urea powder was put into a crucible with a lid and then calcined for 3 h at 550 ^oC in a furnace. The obtained pale yellow powder was collected for further use without additional treatment (Qamar et al., 2021).

3.5 Synthesis of Ba-ZnO/g-C_3N_4 NCs

To prepare the (10%, 20%, 30%, 40%, 50%, and 60%) g-C_3N_4/Ba-ZnO NCs, a weighed amount of 0.1M Ba-doped ZnO NPs, and g-C_3N_4 was added to a 500 mL flask containing 200 mL distilled water to prepare a mixture. This mixture was stirred for 30 min to form a homogeneous solution. The prepared NCs were separated through decantation and then washed three times with distilled water. After washing, the precipitates were dried at 100 ^oC in a vacuum oven for 8 h. The g-C_3N_4/Ba-ZnO NCs were employed for subsequent experiments after grinding to a fine powder (Sher, Javed, Shahid, et al., 2021b).

3.6 Characterization

The crystallinity of the samples was evaluated by using an X-ray diffractometer (XRD-700 Shimadzu Co., Japan, λCuK1 = 0.15406 nm, tube voltage 40 kV, current 30 Ma), and the morphology of the synthesized samples was studied via scanning electron microscopy (SEM) (SEM, JSM 6000). The optical properties of the synthesized samples were studied with a UV-vis-diffuse reflectance spectrometer (UV-3600 Shimadzu Co., Japan). Fourier transform infrared (FTIR) spectra were also used to confirm the formation of NPs, NCs, and the presence of any functional group (FT/IR-6600 Co, Jasco).

3.7 Photocatalytic activity

All the synthesized nanomaterials were assessed for their photocatalytic performance through the degradation of MB dye. In this study, anhydrous MB dye was used to prepare the test solutions. For the effective degradation of MB dye, the as-synthesized nanomaterials were added to a 50 mL solution of MB. Before sunlight illumination, the suspension was continuously stirred under dark conditions for about 30 minutes to develop an adsorption-desorption equilibrium between MB dye and photocatalyst. Then, the stable aqueous dye solution was exposed to sunlight illumination. Then after a certain time of irradiation, the solution was filtered and the absorption spectrum of decomposed dye was collected using a UV–visible spectrophotometer. Finally, the photocatalytic degradation efficiencies of the samples were calculated using the following equation (Sher, Javed, Shahid, et al., 2021b).

$$\text{Photodegradation}(\%) = \frac{(C_o - C_t)}{C_o} \times 100 \qquad (10)$$

Where C_o and C_t denote the initial concentration of dye solution and concentration of dye at a certain reaction time, respectively. Experiments were also carried out to investigate the effects of some factors that influence the photocatalytic process.

3.7.1 Effect of pH

The effect of pH was studied at the pH values of 3-12 at the interval of each time using 50 mL MB solution with a fixed concentration of 20 mg/L and by treating it with 0.1 g of the photocatalyst at room temperature. The acidic and alkaline pH of the media was maintained by adding 0.1 M HCl and 0.1 M NaOH solutions using a pH meter. The concentration of MB free of any suspended photocatalyst was estimated by measuring its absorbance at 664 nm using a UV-vis spectrophotometer. While carrying out the pH experiments the parameters such as irradiation time and photocatalyst dosage were kept constant. Finally, the percentage photodegradation of MB dye was calculated and the plot of percent removal of MB dye versus pH was plotted (Boruah et al., 2016).

3.7.2 Effect of initial dye concentrations

The effect of initial dye concentrations on the extent of photocatalytic degradation of MB on the synthesized NMs was studied by taking 50 mL of the diluted stock solutions of MB 10, 20, 30, 40, and 50 mg/L using 0.1 g of the synthesized photocatalyst at each time. After the photocatalytic experiment was done, the concentration of MB solution free of any suspended photocatalyst was estimated by measuring its absorbance at 664 nm using a UV-vis spectrophotometer. All other parameters were kept constant. Finally, the percentage photodegradation of MB dye was calculated and the plot of percent removal of MB versus initial concentrations of the dye was plotted (Boruah et al., 2016).

3.7.3 Effect of amount of catalyst

To study the effect of the amount of catalyst on dye degradation, a different set of amounts of catalysts was investigated. 0.1 g, 0.2 g, 0.3 g, 0.4 g, and 0.5 g of NC were used with fixed concentrations of MB. After the photocatalytic experiment was done, the concentration of MB solution free of any suspended catalyst was estimated by measuring its absorbance at 664 nm using a UV-vis spectrophotometer. Then, the percentage photodegradation of MB dye was calculated and the plot of percent removal of MB versus initial concentrations of the dye was plotted (Boruah et al., 2016).

3.8 Antibacterial study

The antibacterial activity of the as-synthesized NMs was studied against Gram-positive and Gram-negative bacteria. The antibacterial activity was investigated using the standard disc diffusion method. The bacterial strains that were used for the antibacterial study were *Escherichia coli, Pseudomonas aeruginosa, Staphylococcus aureus, and Streptococcus pyogen*. The first step was the preparation of the agar solution followed by its sterilization. After sterilization, the agar solution was poured into the previously sterilized Petri dishes in a laminar flow chamber. The dishes were left under the laminar flow until the media was semi-solidified. Then, 1 mL of inoculum was added to each dish and shaken gently. Then the Petri dishes were allowed to solidify completely. Afterward, wells were created in these Petri dishes using a steel borer. For each bacterium, the same procedure was repeated (Sher, Javed, Shahid, et al., 2021a). Negative and positive controls were also used, where sterilized distilled water was used as the negative control, and ampicillin trihydrate was used as the positive control. For sample placement, a micro-syringe was used. For the antibacterial study, the Petri dishes were left for 24 h at room temperature in an incubator. After 24 h, the plates were taken out from the incubator, and the inhibition zones were measured using a millimeter ruler.

4. Result and Discussion

4.1 XRD Analysis

The phase purity and crystallinity of pure ZnO, Ba-ZnO, g-C_3N_4, g-C_3N_4/ZnO, and g-C_3N_4/Ba-ZnO were examined by X-ray diffraction method (Figure 8). The XRD patterns of ZnO with its characteristic peaks of the wurtzite hexagonal structure are visibly shown in the graphs indicating the conservation of the ZnO lattice configuration. Different peaks were observed at 2Ɵ values of 31.8, 34.46, 36.3, 47.58, 56.64, 62.9, 66.4, 67.98, 68.16, 69.1, and 69.3 which match the (100), (002), (101), (102), (110), (103), (100), (112), (201), (004), and (202) crystalline plane of ZnO, respectively. The values match precisely with the standard data (JCPDS No 36-1451). All XRD patterns of the NMs showed the existence of ZnO peaks, however, new peaks have emerged in the composite nanomaterials evidencing the incorporation of Ba and g-C_3N_4 into the binary and ternary nanocomposites. Extra peaks were observed on the Ba-ZnO NPs at 2θ values of 24.29, 42.07, and 44.92 compared to pure ZnO NPs which correspond to crystal planes (101), (112), and (103), respectively. These peaks indicate the presence of Ba^{2+} metal (JCPDS No 89-8425) (A Modwi et al., 2019). The emergence of Ba phase is an indication that the Ba ratio has surpassed its maximum solubility in ZnO (Murali & Sohn, 2018). Considering the XRD pattern observed for Ba-ZnO NPs, it was proposed that the incorporation of Ba into the ZnO lattice successfully occurred either in the form of an interstitial atom or as a substitute for Zn^{2+} ions. It was also notable that the ionic radii of the Zn^{2+} (0.72 Å) and Ba^{2+} (1.35 Å) ions were not comparable. Thus, the incorporation of Ba ions occurs only in the interstitial sites of the ZnO lattice as a result of their ionic radii mismatch (Sher, Khan, et al., 2021). As shown in Table 4, a decrease in crystallite size was observed for the Ba^{2+}doped samples compared to pure ZnO, which is attributed to the inclusion of dopant into the Zn sites (N'KONOU et al., 2016).

For pure g-C_3N_4, two diffraction peaks that appeared at 27.6 and 13.1 can be observed. The strong peak at 27.6 is indexed for graphitic materials as (002) planes and the weak peak at 13.1 is indexed for graphitic materials as (100) (Hakimi-Tehrani et al., 2021). A weak diffraction peak of g-C_3N_4 at 27.6 and 27.8 can be observed for g-C_3N_4/ZnO and g-C_3N_4/Ba-ZnO NCs respectively, which indicated the existence of g-C_3N_4 component in the composites. It can be observed from figure 8 that the peak intensities that indicate the presence of g-C_3N_4 in g-C_3N_4/ZnO and g-C_3N_4/Ba-ZnO NCs became much weaker than that in the pure g-C_3N_4, which may be caused by the smaller

amount and uniform dispersion of g-C_3N_4 in both NCs (Nie et al., 2018). Moreover, in the g-C_3N_4/Ba-ZnO NC, very weak peaks at 2Θ values of 23.8, 42.1, and 45 confirmed the presence of the Ba phase in the ternary NC. The position and shapes of ZnO and g-C_3N_4 XRD characteristic peaks for the Ba-ZnO/g-C_3N_4 composite are unchanged compared with those of ZnO and g-C_3N_4. This indicates that the attachment with g-C_3N_4 does not influence the lattice structure of ZnO which is advantageous for the photocatalytic activity of as-synthesized nanocomposite.

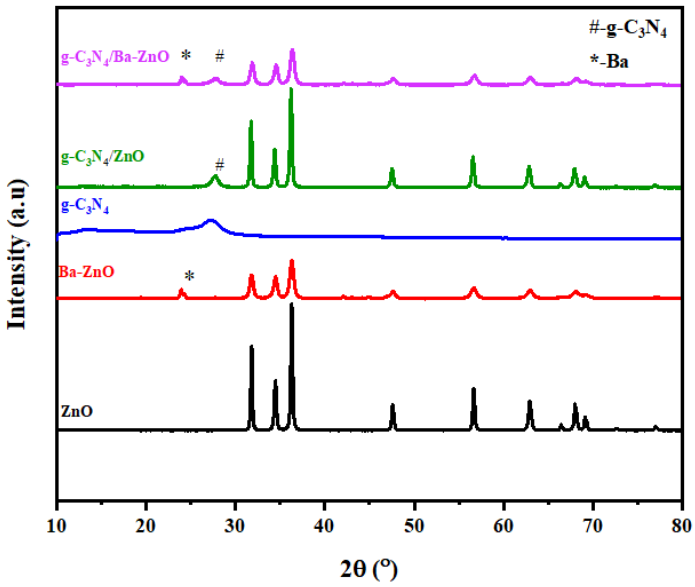

Figure 8: XRD patterns for pure ZnO, 0.1 M Ba-ZnO, g-C_3N_4, g-C_3N_4/ZnO, and 50% g-C_3N_4/Ba-ZnO.

Scherrer's equation was applied to calculate the average crystallite size of the prepared samples (Gawade et al., 2017):

$$D = \frac{K\lambda}{\beta cos\theta} \qquad (11)$$

where K is Scherrer's constant, which is 0.9, λ is the wavelength of the X-ray radiation which is 0.15406 nm, β is peak width at half maximum, and θ is Bragg's angle. Hence, the average crystallite for all samples was calculated and reported in Table 4. By knowing the crystallite size the dislocation density (δ) was determined using Williamson and Smallman's formula equation 12 (Abirami et al., 2020).

$$\delta = \frac{1}{D^2} \qquad (12)$$

where D is the average crystallite size of the prepared samples.

The Microstrain (ε) of the prepared NMs was also calculated using equation 13.

$$\varepsilon = \frac{\beta}{4tan\theta} \quad (13)$$

where β is peak width at half maximum and θ is Bragg's angle.

The values of dislocation density and microstrain were found to be increased with the Ba doping and g-C_3N_4 coupling in table 4. As per the calculated results, the dislocation density and microstrain values were increased with a decrease in crystallite size. The value of δ and ε for Ba-doped ZnO, g-C_3N_4/ZnO, and g-C_3N_4/Ba-ZnO is found to be higher than the pure ZnO NPs, which might be influenced by the inclusion of dissimilar materials in the crystal symmetry that resulted in the increased number of defects in the crystal system of ZnO (Jayaram et al., 2016).

Table 4: Average crystalize size of as-synthesized NMs

Sample No	Sample	Particle size D (nm)	Dislocation density (δ)	Micro strain (ε)
1	Pure ZnO	28.76	1.220876	0.003082
2	0.1 M Ba-ZnO	14.47	9.612464	0.00789
3	g-C_3N_4	6.19	26.09882	0.02351
4	g-C_3N_4/ZnO	24.14	3.064689	0.004815
5	50% g-C_3N_4/Ba-ZnO	11.61	10.89934	0.009877

4.2 SEM Analysis

Figure 9 shows the SEM micrographs of pure and Ba-doped ZnO NPs. It is noticed that the addition of Ba metal into ZnO NPs resulted in increased agglomeration of the Ba-ZnO NPs. The SEM images of the Ba-doped ZnO NPs exhibited a cotton-like porous structure which is favorable for increasing the interaction between the photocatalyst surface and the organic pollutant that leads to enhancing the photodegradation efficiency. The SEM images showed different morphologies of pure and Ba-doped ZnO NPs and nanostructural homogeneities. The SEM result showed the

presence of agglomerated nanospheres. To that purpose, rough morphology was found in figure 9b.

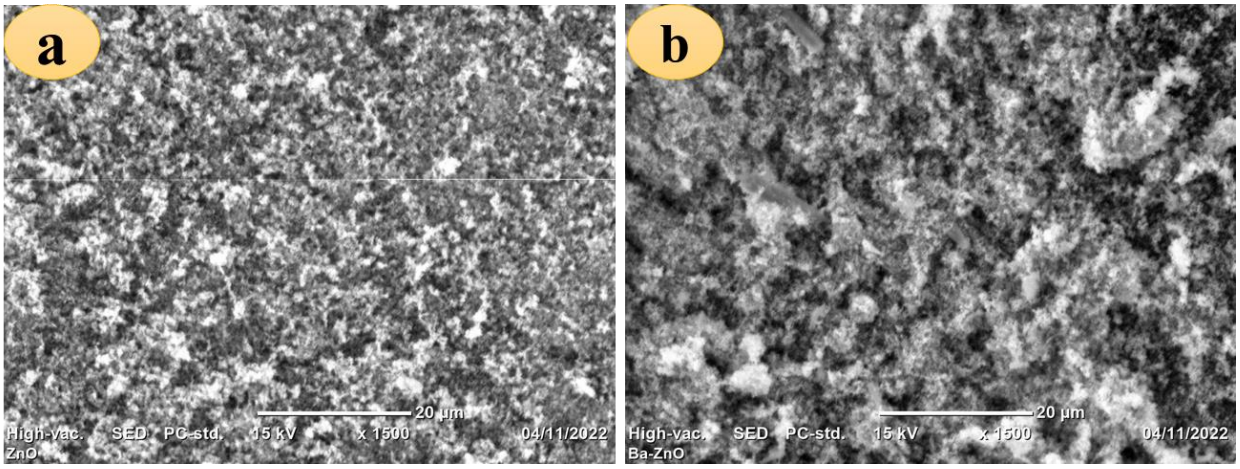

Figure 9: SEM images for a) pure ZnO b) 0.1 M Ba-ZnO

Figure 10 shows the SEM micrographs of g-C_3N_4, g-C_3N_4/ZnO, and g-C_3N_4/Ba-ZnO. As shown in Figure 10c, the pure g-C_3N_4 appears to be aggregated particles containing a large number of irregular smaller crystals, which contributes to its low photocatalytic activity under visible light irradiation (Liu et al., 2012). From Figure 10d and e, it is clearly seen that the NCs display mainly sphere-like agglomerate, which was caused due to anisotropic growth of crystal from the driving force of the dopant and g-C_3N_4 material on ZnO lattice (Javid et al., 2016). The morphology exhibited by g-C_3N_4/ZnO photocatalyst consists of stacked irregular two-dimensional sheets with slight curls (Figure 10d). The degree of agglomeration was prominent in g-C_3N_4/ZnO and g-C_3N_4/Ba-ZnO as compared to thin sheets of g-C_3N_4. The ternary photocatalyst g-C_3N_4/Ba-ZnO displayed the sheet structure with agglomeration. The composite sheets appear thin and transparent and have diverse morphologies (Qamar et al., 2021). The disappearance of discrete ZnO nanoparticles was due to the wrapping or dispersion of ZnO particles with g-C_3N_4 sheets, which have resulted in irregularly agglomerated random-shaped particles.

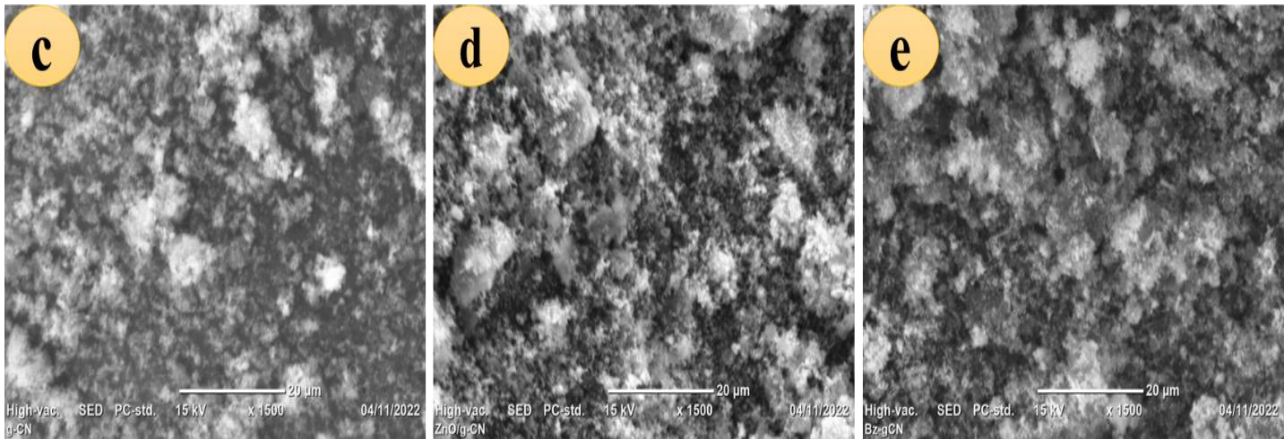

Figure 10: SEM images for c) g-C_3N_4, d) g-C_3N_4/ZnO, and e) 50% g-C_3N_4/Ba-ZnO

4.3 Optical studies

All the synthesized samples were analyzed via UV–visible diffuse reflectance spectroscopy (UV–vis DRS), and their Tauc plots were drawn using the standard procedure and mathematical calculations (Figure 11). The as-synthesized NMs' band gap energy was calculated using the Tauc equation (Tauc et al., 1966):

$$(F(R) \cdot h\upsilon)^n = A \cdot (h\upsilon - E_g) \quad (14)$$

where F(R) is the percentage of reflected light, h is Planck's constant, ν is incident light frequency, E_g is the bandgap energy, A is a proportionality constant and n is the power index that is related to the characteristics transition in a semiconductor (n=1/2). The optical bandgap energy of the NMs was estimated by plotting the $(F(R)\cdot h\upsilon)^n$ versus the photon energy (hυ) and extrapolating the linear region of the curve to the energy axis. The absorption spectra and Tauc plots of the pure ZnO, Ba-ZnO, g-C_3N_4, g-C_3N_4/ZnO, and g-C_3N_4/Ba-ZnO NMs are presented in Figure 11 (a and b).

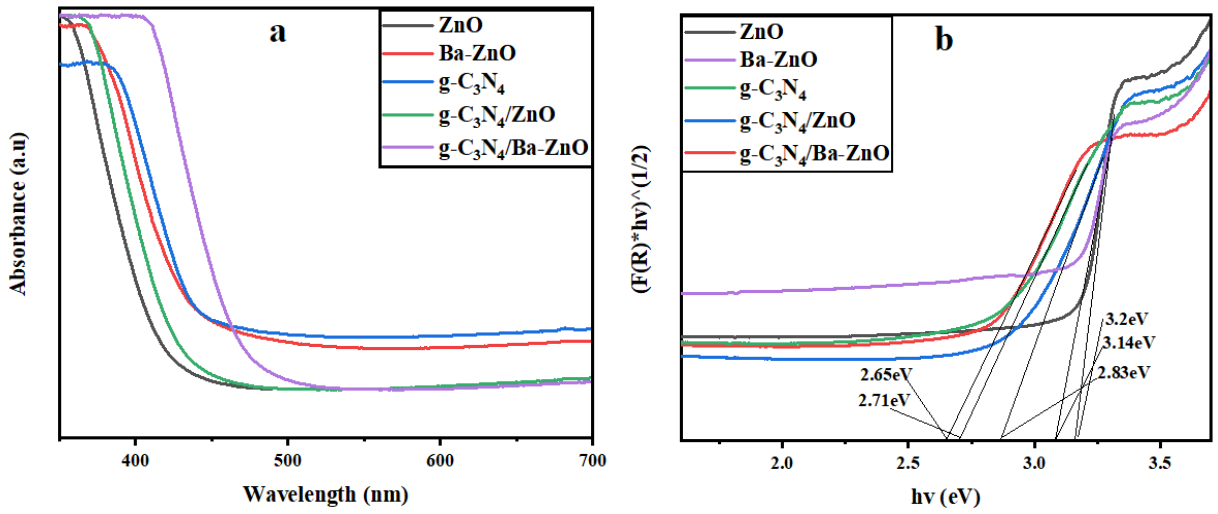

Figure 11: UV–vis spectra (a) and Tauc Plots (b) of pure ZnO, 0.1 M Ba-ZnO, g-C_3N_4, g-C_3N_4/ZnO, and 50% g-C_3N_4/Ba-ZnO

From the graph of UV–Visible spectra, it can be seen that the absorption edge of pure ZnO is around 400nm which limits its absorption capacity in the visible region of the spectrum. However, Ba-ZnO, g-C3N4, g-C_3N_4/ZnO, and g-C_3N_4/Ba-ZnO, exhibited a strong absorption range in the Visible region. This indicates that the introduction of Ba and g-C_3N_4 creates additional states in the bandgap of ZnO, which resulted in the redshift of the absorption edge of the nanocomposites (Gawade et al., 2017). Moreover, among the modified nanocomposites 50% g-C_3N_4/Ba-ZnO exhibited stronger absorption peaks around 435nm. This significant shift to the visible light region may be ascribed to the synergetic effect of Ba^{2+} and g-C_3N_4 on the ZnO NPs. This red-shift in absorption edge of the g-C_3N_4/Ba-ZnO would significantly affect the utilization range of sunlight and make more efficient use of visible light, which as a result enables the NCs to degrade pollutants efficiently under sunlight irradiation (Qamar et al., 2021).

The bandgap energy of the pure ZnO NPs was found to be 3.20 eV which is also consistent with the values reported in the literature (A Modwi et al., 2019). The bandgap energy value of the g-C_3N_4 was found to be 2.71 eV, which is the same as that reported in the literature (Qamar et al., 2021). The bandgap values of pure ZnO NPs and g-C_3N_4 indirectly confirmed their successful synthesis in the desired nanoform. Similarly, the bandgap value of Ba-ZnO, g-C_3N_4/ZnO, and g-C_3N_4/Ba-ZnO NCs was also calculated and found to be 3.14 eV, 2.83 eV, and 2.65 eV respectively. The bandgap energies of all the modified ZnO NMs are smaller than the bandgap energy of the

pure ZnO. This means that the hybridization of ZnO NPs with Ba and g-C_3N_4 caused a decrease in its bandgap energy, expanding the utilization range of sunlight. This may be due to the modification of electronic levels of ZnO NPs by Ba doping and g-C_3N_4 coupling. The lower bandgap energy exhibited by the Ba-ZnO composites may be attributed to defects such as oxygen vacancies (V_O), zinc vacancies (V_{Zn}), oxygen interstitials (O_i), and zinc interstitials (Z_{ni}) (A Modwi et al., 2019). Doped Ba occupies interstitial sites in ZnO NPs. More 2p π-electron of nitrogen compared to those of replaced oxygen at the lattice sites create new energy levels between conduction and valence bands of ZnO, thus, decreasing the band gap in zinc oxide (Yarahmadi et al., 2021). Incorporation of g-C_3N_4 indicating that the N-atom in g-C_3N_4 replaces part of the lattice O in ZnO, so that the g-C_3N_4/ZnO, and g-C_3N_4/Ba-ZnO NCs contains a higher concentration of oxygen vacancies (Zhong et al., 2020). The decrease in the bandgap energy of the composite materials can be considered a factor to shift the absorption edge toward the visible light region and enhance the photocatalytic degradation ability of the NMs.

4.4 FTIR analysis

The FTIR spectra of pure ZnO, Ba-ZnO, g-C_3N_4, g-C_3N_4/ZnO, and g-C_3N_4/Ba-ZnO nanomaterials are shown in Figure 12. The Figure shows that ZnO powder has an absorption peak at about 571 cm^{-1}, which belongs to Zn–O bending vibrational mode (Ngullie et al., 2020). The g-C_3N_4 absorption spectra showed peaks at 1401 cm^{-1} and 1453 cm^{-1} are associated with the heptazine-derived repeating units (Sher, Khan, et al., 2021). The absorption peak at 807 cm^{-1} matches the C–N bending vibrations (Sundaram et al., 2017). The absorption peak at 1621 cm^{-1} is attributed to stretching vibration of the C=C and the one at 1246 and 1324 cm^{-1} is attributed to C–N (Ngullie et al., 2020; Sher, Javed, Shahid, et al., 2021b). The spectrum of the g-C_3N_4 also shows a broad absorption band around 3165 cm^{-1} which corresponds to the N-H stretching vibrations (Sher, Khan, et al., 2021).

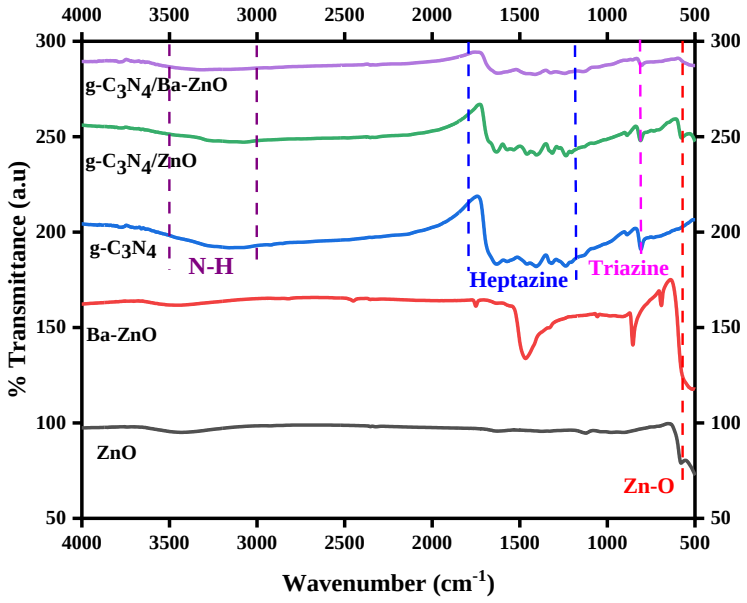

Figure 12: FTIR spectra of pure ZnO, 0.1 M Ba-ZnO, g-C_3N_4, g-C_3N_4/ZnO, and 50% g-C_3N_4/Ba-ZnO

The spectrum of Ba-ZnO shows various absorption bands. In this spectra, an absorption band at the 694 cm^{-1} wavenumber is observed signifying the Zn-O bonding. Moreover, the IR bands attributed to O–H bending at about 1466 cm^{-1} was observed (Arunadevi et al., 2018). Further, a broad absorption peak positioned at 3477 cm^{-1} was owing to the existence of water molecules (S. Wang et al., 2018). In g-C_3N_4/ZnO and g-C_3N_4/Ba-ZnO samples, the strong stretching vibrations of heptazine-based g-C_3N_4 (CN heterocycles) are observed in the 1200−1650 cm^{-1} region. The small absorption band observed at 571 cm^{-1} is associated with the Zn–O bending vibrational mode, which is the same as that observed for the pure ZnO NPs (Ngullie et al., 2020). The vibrational frequency at 807 cm^{-1} is ascribed to the triazine units (Qamar et al., 2021). Thus, FTIR spectra of ZnO, Ba-ZnO, g-C_3N_4, g-C_3N_4/ZnO, and g-C_3N_4/Ba-ZnO NMs are in good agreement with the previous reports confirming their formation without any impurity.

4.5 Photocatalytic optimization studies

All the synthesized nanomaterials were investigated for their photocatalytic activity. The photocatalytic experiments were performed using sunlight. In the first round of photocatalytic degradation experiments, 0.1 g of pure ZnO, pure g-C_3N_4, and Ba-ZnO (0.05 M, 0.1 M, and 0.15 M) NMs were assessed for their photocatalytic activity against MB (20 mg/L), at pH of 8.2 for 90

minutes. The percentage degradation of MB dye of the above-described samples is shown in Figure 13.

It is clear from the Figure shown below that the Ba-doped ZnO NPs have shown higher photocatalytic activity than both pure ZnO and g-C_3N_4. It was further proven that the 0.1 M Ba doped ZnO NCs showed the optimal degradation rate among the doped NPs, which was 94% in just 90 minutes of sunlight irradiation. The percentage of the MB dye degraded using pure ZnO NPs was 76% in 90 min. The reason behind this significant improvement in the photocatalytic activity of Ba-doped ZnO NPs is the extension of the absorbance edge towards the visible region (Khalid et al., 2019). Thus, it can be said that doping ZnO with Ba metal shifted the absorbance edge toward the visible region, as a result, enhances its photocatalytic activity.

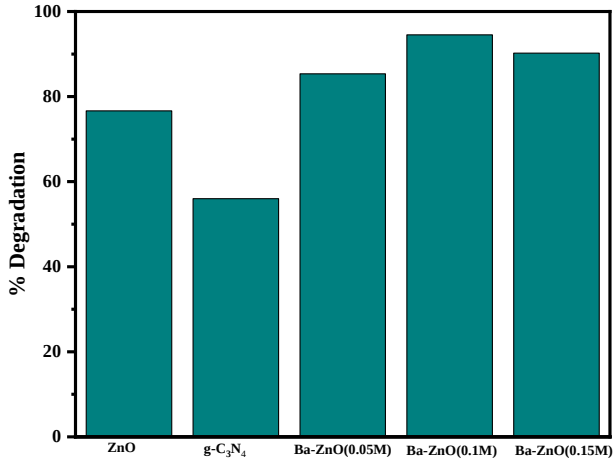

Figure 13: percentage degradation of MB by pure ZnO, pure g-C_3N_4, and Ba-doped ZnO

In the second round of photocatalytic degradation experiments, the binary and ternary NCs which are 50% g-C_3N_4/ZnO and g-C_3N_4/Ba-ZnO (10%, 20%, 30%, 40%, 50%, and 60%) NCs were employed for photodegradation of the MB dye. The percentage degradation of MB dye for the above-described samples is shown in Figure 14. Among the ternary NCs, the 50% g-C_3N_4/Ba-ZnO NCs showed the highest percentage of photocatalytic degradation of MB (98.55%) in just 90 minutes. The enhanced photocatalytic activity of 50% g-C_3N_4/Ba-ZnO NCs is attributed to its lower bandgap (2.65 eV) together with the existence of a longer absorption edge in the visible

region of the spectrum (Sher, Javed, Shahid, Hakami, et al., 2021). Moreover, it resulted due to the improved synergistic effect, upgraded charge transmission between g-C_3N_4 and Ba-ZnO, and inhibition of e-h pair recombination These characteristics lead to enhanced photocatalytic activity 50% g-C_3N_4/Ba-ZnO under sunlight irradiation (Qamar et al., 2021).

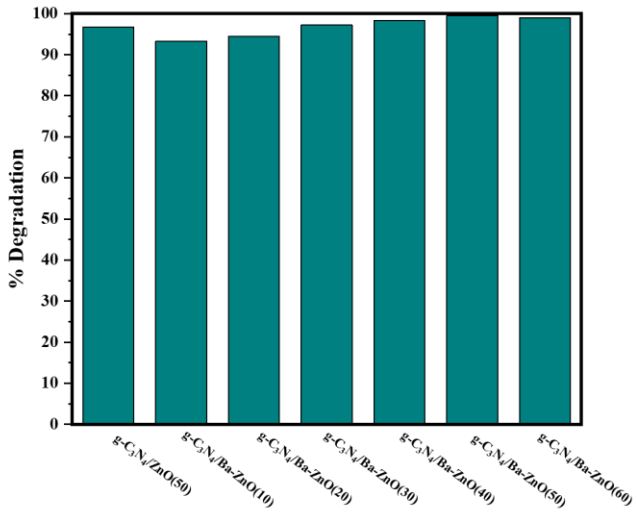

Figure 14: Percent degradation of the MB for the 50% g-C_3N_4/ZnO and (10%, 20%, 30%, 40%, 50%, and 60%) g-C_3N_4/Ba-ZnO NCs

4.5.1 Effect of solution pH

It is widely reported that due to varying interactions between catalyst and pollutant in a different medium, dye solution pH plays a significant role in photodegradation reaction. In this study, the photocatalytic activity of 50% g-C_3N_4/Ba-ZnO NCs was investigated at different pH values (3, 5, 7, 9, and 11) at a fixed catalyst dosage (0.1 g), sunlight irradiation (90 min) and dye concentration (20 mg/L). The pH of the solution was adjusted using 0.1 M NaOH and 0.1 M HCl. The maximum degradation efficiency was observed at pH 9. Degradation efficiency increased with increasing pH. With an increase in the pH value, • OH is easily generated by the reaction between the positive hole and hydroxyl ions; thus, the efficiency for the degradation is also enhanced. However, photodegradation efficiency generally decreased at too high pH (pH $\geq$ 11), as the production of excess hydroxyl ions starts the competition with pollutants to get adsorbed onto the surface of the catalyst and neutralized acidic sites on the photocatalyst (Boruah et al., 2016). Considering MB is a cationic dye molecule, the efficiency of degradation increases up to pH 9 and then decreases.

The maximum degradation of the MB is 98.97%, achieved at pH 9 under the same experimental conditions. The surface properties and the oxygen-containing functionalities of the 50% g-C_3N_4/Ba-ZnO nanocomposite play an important role in the degradation of the dye molecules at different pH of the reaction medium. The results are summarized in Figure 15 below.

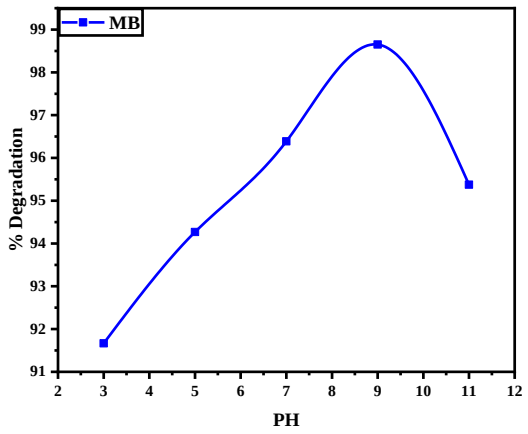

Figure 15: Effect of initial pH on Photodegradation efficiency of MB dye on 50% g-C_3N_4/Ba-ZnO NC.

4.5.2 Effect of catalyst dosage

The influence of the photocatalyst dosage on the degradation of MB using 50% g-C_3N_4/Ba-ZnO NCs was studied by making the amount of photocatalyst 0.1 g, 0.2 g, 0.3 g, 0.4 g, and 0.5 g, Under optimum conditions with an initial MB concentration of 20 mg/L. The results are presented in Figure 16.

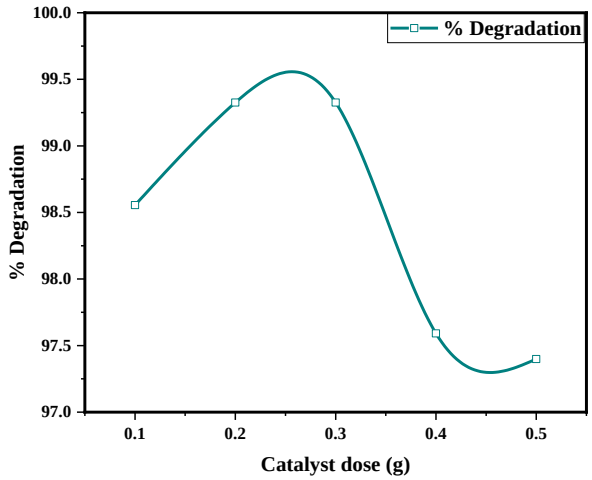

Figure 16: Effect of catalyst dose on Photodegradation efficiency of MB dye on 50% g-C_3N_4/Ba-ZnO NC.

Generally, the amount of photo mineralization of water pollutants increases with an increase in the amount of catalyst dosage. This is due to the exposure of more active sites on the photocatalyst, which adsorb more photons and produces more OH• radicals and positive holes under irradiation. These hydroxyl radicals and positive holes take participate in the photocatalytic reaction, and thus, the rate of degradation of pollutants increases. At a lower dosage of catalyst, most of the irradiated sunlight is directly transmitted from the solution, and a little part of it was consumed by the catalyst to perform. However, a higher dosage of catalyst, beyond a certain limit, decreases the rate of photodegradation of pollutants. One of the possible reasons might be the turbidity of the solution, which increased with the amount of catalyst and blocks the sunlight irradiation inside the solution, and also enhances the light scattering in the suspension which prevents light from reaching some particles, and thus, some of the photocatalyst surfaces becomes unavailable for light absorption (Reza et al., 2017). Therefore, above the optimum amount of catalyst, the degradation efficiency decreases due to the increased opacity of the suspension.

4.5.3 Effect of initial MB concentration

The effect of initial dye concentration was investigated by using 10 mg/L, 20 mg/L, 30 mg/L, 40 mg/L, and 50 mg/L of MB concentration with 0.1 g of 50% g-C_3N_4/Ba-ZnO photocatalyst under sunlight irradiation. The results are shown in Figure 17.

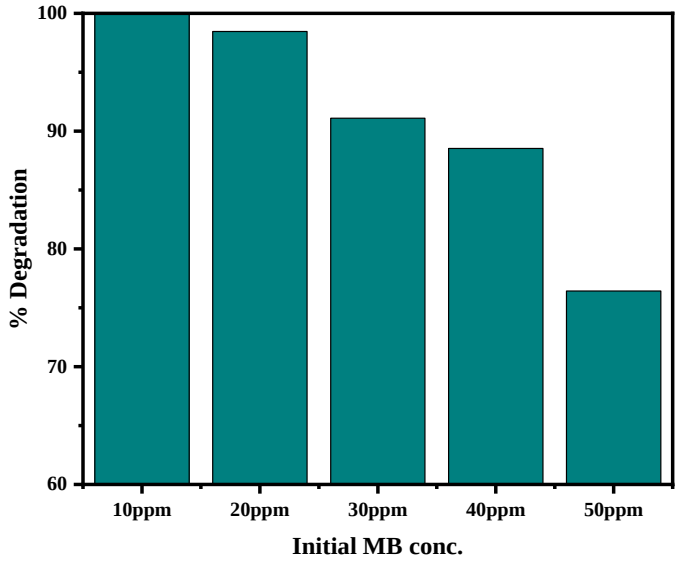

Figure 17: Effect of initial dye concentration on photodegradation efficiency of MB dye on 50% g-C_3N_4/Ba-ZnO NC.

From the bar graph above, the percentage degradation decreases with an increasing amount of MB concentration, and with a constant photocatalyst amount. This phenomenon relates to the unavailability of active sites on the photocatalyst. As the reactive places are filled by the dye molecules, the generation of •OH radicals on the surface of the photocatalyst is diminished, and also the path dimension of the photons arriving in the dye solution reduces as the initial dye concentration increases (Christy et al., 2021). Therefore, the photodegradation system was effective at a lower concentration of MB dye.

4.5.4 Reusability studies

The stability of the synthesized photocatalyst material was evaluated by recycling the photocatalysts for the photocatalytic degradation of the same quantity of fresh MB after each run. In this study, 50% g-C_3N_4/Ba-ZnO nanocomposites were recovered from the solution by centrifugation and washed with ethanol several times. The recycled nanocomposite was used as a photocatalyst for five repetitive experiments. The results are summarized in Figure 18. As shown in the bar graph, the efficiency of the photocatalyst for the removal of MB dye dropped to 93.6%

after 5 consecutive usages. Overall, it can be concluded that 50% g-C_3N_4/Ba-ZnO NCs have good regeneration and reusability potential.

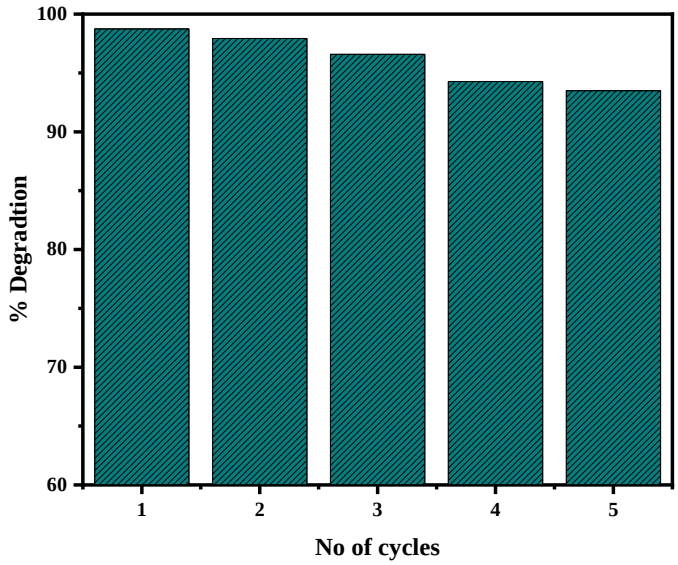

Figure 18: Recycling stability studies for the catalytic degradation of MB dye on 50% g-C_3N_4/Ba-ZnO NCs.

4.5.5 Kinetic studies

To determine whether the photocatalytic degradation mechanism is determined by pseudo first order or pseudo second order kinetics, the plots of ln (C_0/C_t) versus time and t/q_t vs time with a different initial concentration of MB were plotted respectively. In the presence of 50% g-C_3N_4/Ba-ZnO, the absorbance of MB at different time intervals (Figure 19) exhibits continuous decline confirming its high degradation efficiency with a complete photocatalytic degradation in 120 min. The compliance of the experimental data was verified with the pseudo-first-order kinetics model (Balcha et al., 2016):

$$\ln\left(\frac{Ct}{Co}\right) = kt \qquad (15)$$

The removal of the MB by NMs was also examined by pseudo-second-order reaction kinetics (J. Singh et al., 2018).

$$\frac{1}{Ct} = \frac{1}{Co} + k_2 t \qquad (16)$$

Where K is the apparent reaction rate constant (min^{-1}), t is the irradiation time, C_0 is the initial concentration of MB and C_t is the concentration of MB at a reaction time t.

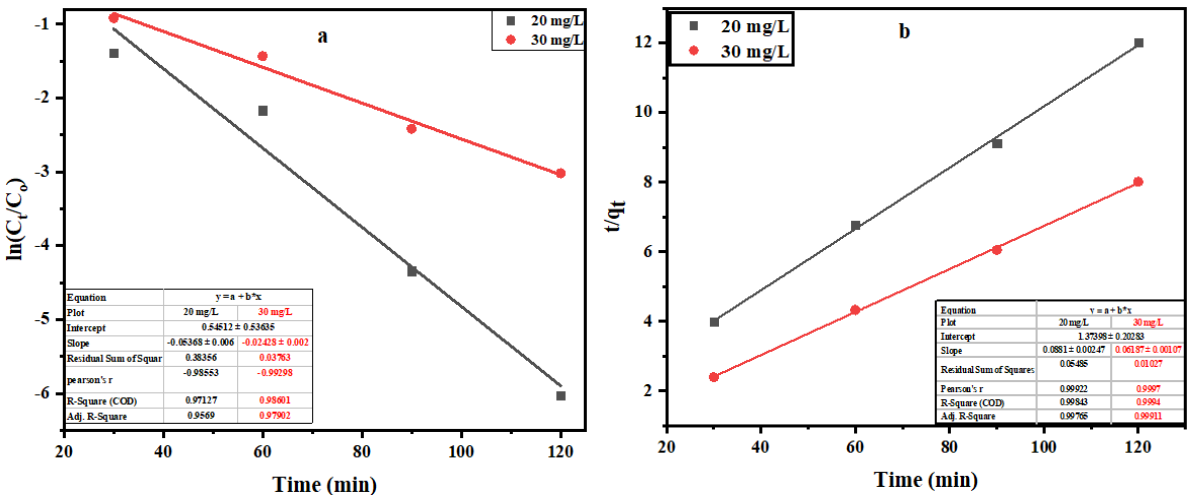

Figure 19: a) Pseudo first-order b) Pseudo second-order kinetics graph of 50% g-C_3N_4/Ba-ZnO NCs for the MB photodegradation

The plot of ln (C_0/C_t) versus time and t/q_t vs time with a different initial concentration of MB is shown in Figure 19 (a and b). The Figure shows that the photocatalytic degradation fully follows the pseudo-second-order kinetics in the case of initial concentrations of 20 and 30 mg/L. The value of R^2 for the pseudo-second-order was higher as compared to the R^2 value of the pseudo-first-order. Therefore, the pseudo-second-order kinetic model is more favorable to describe the degradation kinetics of MB dye by 50% g-C_3N_4/Ba-ZnO. A good agreement between this model and experimental data is indicated by the large correlation coefficients 0.9984 and 0.9994 for 20 and 30 mg/L respectively for 50% g-C_3N_4/Ba-ZnO. This confirmed the applicability of the pseudo-second-order reaction kinetic model for MB photocatalytic degradation. The calculated rate constant (k_2) data obtained from the slope of t/q_t vs time linear plots are $4.92 * 10^{-3}$ and $2.77 * 10^{-}$

^{3} for 20 and 30mg/L of MB, respectively. Moreover, it was observed that the degradation rate of MB decreases with the increase in initial dye concentration over the studied concentration range.

4.5.6 Photodegradation mechanism

Based on the above results, a possible mechanism for the g-C_3N_4/Ba-ZnO NCs under sunlight irradiation was proposed. As we know, the coupling of two semiconductors will construct heterojunctions at the interface. And the formed heterojunctions are beneficial for the efficient interface charge carrier separation between them. Two types of charge transfer mechanisms can be used to explain the improved separation, which are type-II heterojunction and direct Z-scheme heterojunction systems. If the former were to be the mechanism of this enhanced photocatalytic degradation system, the photogenerated electrons in the g-C_3N_4 move from its CB into the CB of Ba-ZnO when exposed to light, the photogenerated holes in the VB of Ba-ZnO can transfer to the VB of g-C_3N_4 (Hakimi-Tehrani et al., 2021). This charge transfer mechanism does efficiently separate the photogenerated charge carriers, but the redox abilities of electrons and holes were reduced, thermodynamically unfavorable for the photocatalytic reactions. In the direct Z-scheme mechanism, electrons and holes with relatively higher reduction and oxidation ability were well preserved. Under sunlight irradiation, the CB of g-C_3N_4 contains photogenerated electrons while its holes remained at its VB. The electrons at CB of Ba-ZnO recombine with the photogenerated holes present at VB of g-C_3N_4 (Figure 20). This leads to efficient separation of charge carriers. As a result, the electrons available at CB of g-C_3N_4 are trapped by molecular oxygen to obtain reactive superoxide radicals ($\cdot O_2^-$) which directly oxidize the MB dye molecules. Since the standard redox potential of ZnO is more positive than that of $\cdot OH/H_2O$, the radicals could not be generated on the VB of g-C_3N_4 but on the VB of Ba-ZnO via water oxidation by holes (Li et al., 2018; Nie et al., 2018). The generated highly reactive hydroxyl radical species ($\cdot OH^-$) on the VB of Ba-ZnO are responsible for the degradation of MB dye molecules into harmless products (Sher, Khan, et al., 2021). This indicated that the transfer of photogenerated electrons and holes did not follow the traditional double-charge rule. Instead, the electrons (e^-) on CB of Ba-ZnO transferred to VB of g-C_3N_4 with potential difference as driving force, leaving e^- on CB of g-C_3N_4 and holes (h^+) on VB of Ba-ZnO.

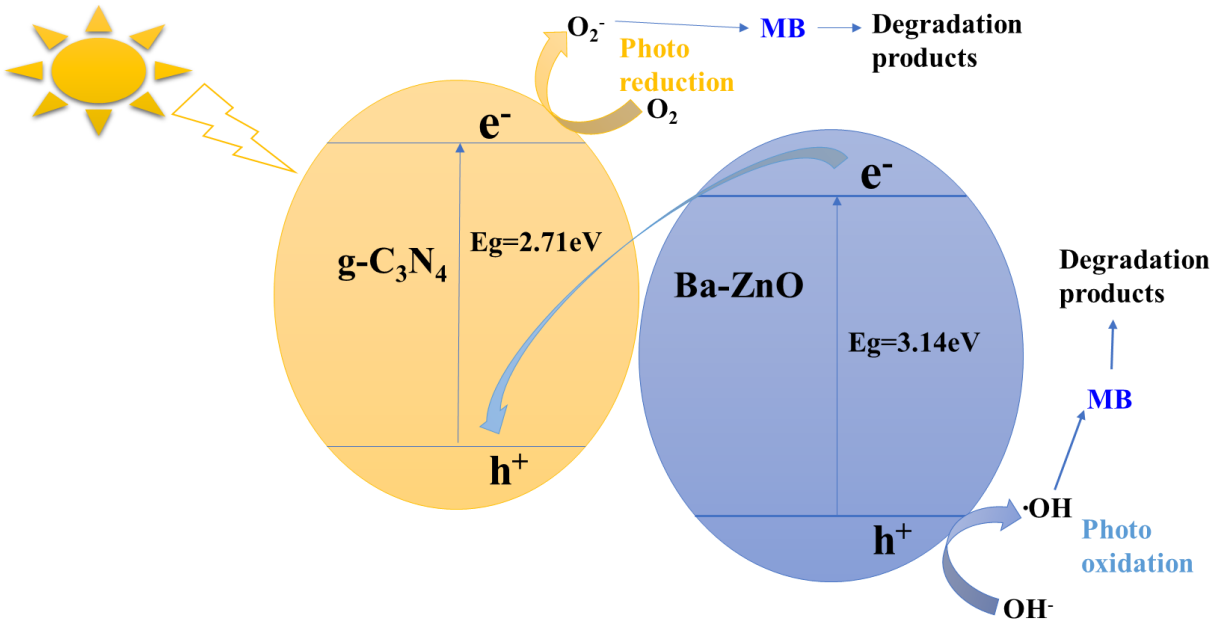

Figure 20: Proposed Z-scheme photodegradation mechanism for enhanced photocatalytic features of MB over synthesized g-C_3N_4/Ba-ZnO NCs under sunlight irradiation.

In an ideal photocatalytic process, MB dye molecules are mineralized into carbon dioxide (CO_2) and water (H_2O) in the presence of g-C_3N_4/Ba-ZnO NCs and reactive oxidizing species, the relevant reactions are listed in Equations below.

$$g\text{-}C_3N_4/Ba\text{-}ZnO + \text{sunlight irradiation} \longrightarrow g\text{-}C_3N_4/Ba\text{-}ZnO\ (e^- + h^+) \quad (17)$$

$$g\text{-}C_3N_4\ (e^-) + O_2 \longrightarrow \cdot O_2^- \quad (18)$$

$$Ba\text{-}ZnO\ (h^+) + H_2O \longrightarrow \cdot OH + H^+ \quad (19)$$

$$\cdot O_2^- + e^- + 2H^+ \longrightarrow H_2O_2 \quad (20)$$

$$H_2O_2 + e^- \longrightarrow \cdot OH + OH^- \quad (21)$$

$$\cdot OH + C_{16}H_{18}ClN_3S\ (MB) \longrightarrow CO_2 + H_2O \quad (22)$$

$$\cdot O_2^- + C_{16}H_{18}ClN_3S\ (MB) \longrightarrow CO_2 + H_2O \quad (23)$$

4.6 Antibacterial studies

The antibacterial activity of the as-synthesized NMs was studied against Gram-positive and Gram-negative bacteria. The antibacterial activity was investigated using the standard agar diffusion

method. The antibacterial study was performed against four bacterial strains (*Escherichia coli, Pseudomonas aeruginosa, Staphylococcus aureus, and Streptococcus pyogen*). The positive control (Ampicillin) was applied against all the pathogens. While comparing the gram-positive and gram-negative bacteria, it has been observed that the inhibition zone is higher in gram-positive (*S. aureus and S. pyogen*) bacteria than those of gram-negative bacteria (*E. coli and P. aeruginosa*) (Table 5). This may be due to the difference in their different structure and the chemical composition of the cell surface. Gram-positive bacterial strains are species with thick peptidoglycan layer which is relatively porous, allowing substances to pass through them quite easily. In gram-negative bacteria, this peptidoglycan layer is greatly reduced and is further protected by a second, outer membrane (Bhuyan et al., 2015).

Table 5: Zone of inhibition (mm) of as-synthesized NMs against gram-positive and gram-negative bacteria at concentrations of 75 and 100 µg/mL.

Sample NMs	Conc. (µg/mL)	Bacteria Species and Zone of Inhibitions in mm			
		E. coli	*P. aeruginosa*	*S. aureus*	*S. pyogen*
g-C_3N_4	75	6.5	6.5	7	7
	100	7	7	7.5	8
ZnO	75	7.5	7	8	8.5
	100	9	8	9	9
Ba-ZnO	75	8	8	9	9.5
	100	10	9	11	11
ZnO/g-C_3N_4	75	9	9	9.5	10
	100	11	10.5	12	11.5
Ba-ZnO/g-C_3N_4	75	10	10	10.5	11
	100	11.5	11	12	12.5
Ampicillin (+ve control)		13.5	13	14	14.5

The zone of inhibition values for all NMs was measured as shown in Figure 21 and the results are given in Table 5. The Table indicates that all the synthesized NMs have shown antibacterial activity against all four pathogens studied. The zones were increased with respect to the modifications applied to ZnO NPs. From these zone measurements, it could be stated that g-C_3N_4/Ba-ZnO nanocomposites possess relatively higher antibacterial activity, compared to the other synthesized NMs. Pure g-C_3N_4 showed the minimum zone of inhibition against *E. coli* and

P. aeruginosa which is 6.5 mm and 7 mm against *S. aureus* and *S. pyogen* (G+). Relative to g-C_3N_4, pure ZnO NPs showed a better zone of inhibitions ranging from 7 mm to 9.5 mm. Furthermore, 0.1 M Ba doped ZnO exhibited improved antibacterial activity than both g-C_3N_4 and pure ZnO NPs with the highest zone of inhibition recorded at 100 µg/mL against *S. aureus* and *S. pyogen* which is 11 mm. This is due to the generation of reactive oxygen species (ROS) due to the synergistic effect of ZnO and Ba loading and also could be the abrasive surface texture of ZnO as doping of transition metals increases the surface defects (Sharma et al., 2016). The ROS generation is attributed to the creation of photoinduced charge carriers in ZnO NPs and their interactions with oxygen and water molecules on the surface of particles. 50% g-C_3N_4/ZnO and 50% g-C_3N_4/Ba-ZnO also exhibited higher zones of inhibition compared to other synthesized NMs. However, the ternary composite has shown the highest zones of inhibition against all bacterial strains. The highest zone of inhibition by the ternary NC was recorded against gram-positive bacteria *S. pyogen* which is 12.5 mm. The antibacterial activity of the 50% g-C_3N_4/Ba-ZnO NC was compared with ampicillin as the positive control and found to have comparable values.

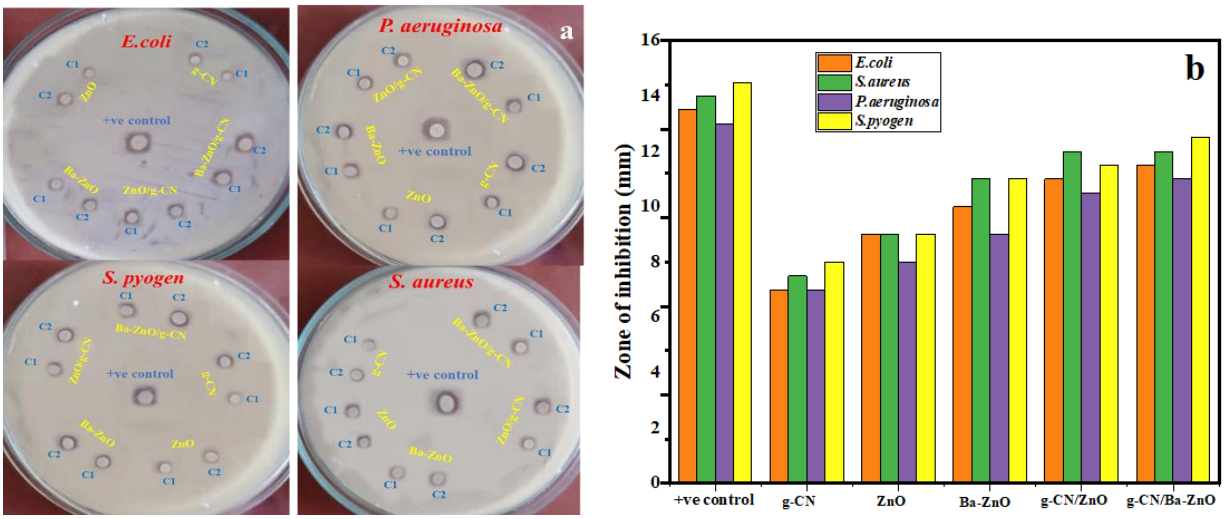

Figure 21: The antibacterial activity of the NMs against G+ and G- bacterial strains a) Agar plates containing zones of inhibition b) bar graphs representing inhibition zone diameters against various bacterial strains

There are numerous mechanisms behind the antibacterial activity of zinc oxide nanomaterials. Some mechanisms have been proposed and they may involve the generation of ROS, release of Zn^{2+} ions, and damage to cell membranes (Abebe et al., 2020). The possible antibacterial

mechanism of 50% g-C_3N_4/Ba-ZnO NC is the increase in the generation of reactive oxygen species (ROS) due to the reduction of the bandgap of ZnO and the large surface area provided by the g-C_3N_4 for the surface interaction of the NC with the bacterial membrane (Sundaram et al., 2017). Therefore, it could be deduced that the creation of active species by the photoinduced reaction is the main source of bactericidal performance.

5. Conclusion and Recommendations

The various nanomaterials which are pure ZnO, pure g-C_3N_4, Ba-ZnO (0.05 M, 0.1 M, and 0.15 M), 50% g-C_3N_4/ZnO, and g-C_3N_4/Ba-ZnO (10%, 20%, 30%, 40%, 50%, and 60%) NCs were synthesized through facile methods. The as-synthesized NMs were characterized by XRD, FTIR, UV-vis-DRS, and SEM. XRD analysis disclosed the formation of hexagonal crystalline nanoparticles with ZnO wurtzite crystal structure. The UV-DRS studies revealed that bandgap energy of ZnO was significantly decreased from 3.2 eV to 2.65 eV after doping it with Ba and coupling it with g-C_3N_4. The FTIR spectra of g-C_3N_4/Ba-ZnO NCs showed the strong stretching vibrations of heptazine-based CN heterocycles in the 1200−1650 cm^{-1} region and bending vibration mode of Zn-O at 571 cm^{-1} which manifests the successful formation of heterojunction between Ba-ZnO and g-C_3N_4. In the first round of photocatalytic studies, the pure ZnO, pure g-C_3N_4, and (0.05 M, 0.1 M, and 0.15 M) Ba-ZnO were assessed for their photocatalytic activity. Then the 0.1M Ba-ZnO NPs exhibited higher photocatalytic efficiency. Afterward, the pure ZnO and 0.1 M Ba doped ZnO NMs were coupled with pure g-C_3N_4 in different ratios and assessed for their photocatalytic activities. Among these NMs, 50% g-C_3N_4/Ba-ZnO composites exhibited higher photocatalytic degradation efficiency compared with the other synthesized NMs. Different parameters affecting the photocatalytic degradation of MB were also studied. The obtained results reveal that the 50% g-C_3N_4/Ba-ZnO composites can effectively degrade 98.55% of MB dye within just 90 min under sunlight irradiation which is greatly superior to that of pure ZnO and pure g-C_3N_4. The enhanced photocatalytic activity of 50% g-C_3N_4/Ba-ZnO could be attributed to the effective separation and transportation of the photogenerated charge carriers, greater surface area, and extended visible light response in g-C_3N_4/Ba-ZnO NCs. The antibacterial analysis showed that the 50% g-C_3N_4/Ba-ZnO NCs were the most effective compared to other synthesized NMs. Thus, on account of the remarkable photocatalytic activity and antibacterial performance of the 50% g-C_3N_4/Ba-ZnO NCs, it may be applied for the bacterial disinfection of wastewater and the photodegradation of numerous organic pollutants.

Forthcoming studies could consider the characterization of the synthesized NMs to determine their chemical composition, particle size, and surface properties by using EDS, TEM, and BET analysis, respectively. Furthermore, the application of the ternary NC in real wastewater samples should also be investigated for the removal of MB and the simultaneous removal of other pollutants.

References

Abbas, K. N., & Bidin, N. (2017). Morphological driven photocatalytic activity of ZnO nanostructures. *Applied Surface Science, 394*, 498-508.

Abdel-Wahab, M. S., Jilani, A., Yahia, I., & Al-Ghamdi, A. A. (2016). Enhanced the photocatalytic activity of Ni-doped ZnO thin films: Morphological, optical and XPS analysis. *Superlattices and Microstructures, 94*, 108-118.

Abdi, J., Vossoughi, M., Mahmoodi, N. M., & Alemzadeh, I. (2017). Synthesis of metal-organic framework hybrid nanocomposites based on GO and CNT with high adsorption capacity for dye removal. *Chemical Engineering Journal, 326*, 1145-1158.

Abebe, B., Zereffa, E. A., Tadesse, A., & Murthy, H. (2020). A review on enhancing the antibacterial activity of ZnO: Mechanisms and microscopic investigation. *Nanoscale research letters, 15*(1), 1-19.

Abirami, N., Arulanantham, A., & Wilson, K. J. (2020). Structural and magnetic properties of cobalt doped ZnO thin films deposited by cost effective nebulizer spray pyrolysis technique. *Materials Research Express, 7*(2), 026405.

Adam, R. E., Pozina, G., Willander, M., & Nur, O. (2018). Synthesis of ZnO nanoparticles by co-precipitation method for solar driven photodegradation of Congo red dye at different pH. *Photonics and Nanostructures-Fundamentals and Applications, 32*, 11-18.

Adegoke, K. A., & Bello, O. S. (2015). Dye sequestration using agricultural wastes as adsorbents. *Water resources and industry, 12*, 8-24.

Ai, L., Zhang, C., Liao, F., Wang, Y., Li, M., Meng, L., & Jiang, J. (2011). Removal of methylene blue from aqueous solution with magnetite loaded multi-wall carbon nanotube: kinetic, isotherm and mechanism analysis. *Journal of hazardous materials, 198*, 282-290.

Al-Alwani, M. A., Ludin, N. A., Mohamad, A. B., Kadhum, A. A. H., & Mukhlus, A. (2018). Application of dyes extracted from Alternanthera dentata leaves and Musa acuminata bracts as natural sensitizers for dye-sensitized solar cells. *Spectrochimica acta part A: molecular and biomolecular spectroscopy, 192*, 487-498.

Ali, M., Hoque, M., Safdar Hossain, S., & Biswas, M. (2020). Nanoadsorbents for wastewater treatment: next generation biotechnological solution. *International Journal of Environmental Science and Technology, 17*, 4095-4132.

Ando, E., & Miyazaki, M. (2008). Durability of doped zinc oxide/silver/doped zinc oxide low emissivity coatings in humid environment. *Thin Solid Films, 516*(14), 4574-4577.

Aponiene, K., & Luksiene, Z. (2015). Effective combination of LED-based visible light, photosensitizer and photocatalyst to combat Gram (−) bacteria. *Journal of Photochemistry and Photobiology B: Biology, 142*, 257-263.

Arunadevi, R., Kavitha, B., Rajarajan, M., Suganthi, A., & Jeyamurugan, A. (2018). Investigation of the drastic improvement of photocatalytic degradation of Congo red by monoclinic Cd, Ba-CuO nanoparticles and its antimicrobial activities. *Surfaces and Interfaces, 10*, 32-44.

Asahi, R., Morikawa, T., Ohwaki, T., Aoki, K., & Taga, Y. (2001). Visible-light photocatalysis in nitrogen-doped titanium oxides. *science, 293*(5528), 269-271.

Ashebir, M. E., Tesfamariam, G. M., Nigussie, G. Y., & Gebreab, T. W. (2018). Structural, optical, and photocatalytic activities of Ag-doped and Mn-doped ZnO nanoparticles. *Journal of Nanomaterials, 2018*.

Authority, E. F. S. (2005). Opinion of the Scientific Panel on food additives, flavourings, processing aids and materials in contact with food (AFC) to review the toxicology of a number of dyes illegally present in food in the EU. *EFSA Journal, 3*(9), 263.

Avadhut, Y. S., Weber, J., Hammarberg, E., Feldmann, C., & auf der Günne, J. S. (2012). Structural investigation of aluminium doped ZnO nanoparticles by solid-state NMR spectroscopy. *Physical Chemistry Chemical Physics, 14*(33), 11610-11625.

Balcha, A., Yadav, O. P., & Dey, T. (2016). Photocatalytic degradation of methylene blue dye by zinc oxide nanoparticles obtained from precipitation and sol-gel methods. *Environmental Science and Pollution Research, 23*(24), 25485-25493.

Beura, R., Pachaiappan, R., & Thangadurai, P. (2018). A detailed study on Sn4+ doped ZnO for enhanced photocatalytic degradation. *Applied Surface Science, 433*, 887-898.

Bhuyan, T., Khanuja, M., Sharma, R., Patel, S., Reddy, M., Anand, S., & Varma, A. (2015). A comparative study of pure and copper (Cu)-doped ZnO nanorods for antibacterial and photocatalytic applications with their mechanism of action. *Journal of Nanoparticle Research, 17*(7), 1-11.

Boruah, P. K., Borthakur, P., Darabdhara, G., Kamaja, C. K., Karbhal, I., Shelke, M. V., . . . Das, M. R. (2016). Sunlight assisted degradation of dye molecules and reduction of toxic Cr

(VI) in aqueous medium using magnetically recoverable Fe 3 O 4/reduced graphene oxide nanocomposite. *RSC advances, 6*(13), 11049-11063.

Chanu, L. A., Singh, W. J., Singh, K. J., & Devi, K. N. (2019). Effect of operational parameters on the photocatalytic degradation of Methylene blue dye solution using manganese doped ZnO nanoparticles. *Results in Physics, 12*, 1230-1237.

Chaudhary, B., & VIOLET, T. (2020). Chemistry of synthetic dyes: A review. *J. Interdiscipl. Cycle Res, 12*(390), 390-396.

Chen, X., Shen, S., Guo, L., & Mao, S. S. (2010). Semiconductor-based photocatalytic hydrogen generation. *Chemical reviews, 110*(11), 6503-6570.

Chong, M. N., Jin, B., Chow, C. W., & Saint, C. (2010). Recent developments in photocatalytic water treatment technology: a review. *Water research, 44*(10), 2997-3027.

Christoforidis, K. C., Montini, T., Bontempi, E., Zafeiratos, S., Jaén, J. J. D., & Fornasiero, P. (2016). Synthesis and photocatalytic application of visible-light active β-Fe2O3/g-C3N4 hybrid nanocomposites. *Applied Catalysis B: Environmental, 187*, 171-180.

Christy, E. J. S., Amalraj, A., Rajeswari, A., & Pius, A. (2021). Enhanced photocatalytic performance of Zr (IV) doped ZnO nanocomposite for the degradation efficiency of different azo dyes. *Environmental Chemistry and Ecotoxicology, 3*, 31-41.

Constapel, M., Schellenträger, M., Marzinkowski, J. M., & Gäb, S. (2009). Degradation of reactive dyes in wastewater from the textile industry by ozone: Analysis of the products by accurate masses. *Water research, 43*(3), 733-743.

Coronado, J. M., Fresno, F., Hernández-Alonso, M. D., & Portela, R. (2013). *Design of advanced photocatalytic materials for energy and environmental applications*: Springer.

Crini, G. (2006). Non-conventional low-cost adsorbents for dye removal: a review. *Bioresource technology, 97*(9), 1061-1085.

da Silva, F. J. G., & Gouveia, R. M. (2020). Global population growth and industrial impact on the environment *Cleaner Production* (pp. 33-75): Springer.

Danial, E. N., Hjiri, M., Abdel-Wahab, M. S., Alonizan, N., El Mir, L., & Aida, M. (2020). Antibacterial activity of In-doped ZnO nanoparticles. *Inorganic Chemistry Communications, 122*, 108281.

De Gisi, S., Lofrano, G., Grassi, M., & Notarnicola, M. (2016). Characteristics and adsorption capacities of low-cost sorbents for wastewater treatment: A review. *Sustainable Materials and Technologies, 9*, 10-40.

Devi, K. N., Devi, S. A., Singh, W. J., & Singh, K. J. (2021). Nickel doped zinc oxide with improved photocatalytic activity for Malachite Green Dye degradation and parameters affecting the degradation. *Journal of Materials Science: Materials in Electronics, 32*(7), 8733-8745.

Dindar, B., & Güler, A. C. (2018). Comparison of facile synthesized N doped, B doped and undoped ZnO for the photocatalytic removal of Rhodamine B. *Environmental nanotechnology, monitoring & management, 10*, 457-466.

Dong, F., Zhao, Z., Xiong, T., Ni, Z., Zhang, W., Sun, Y., & Ho, W.-K. (2013). In situ construction of g-C3N4/g-C3N4 metal-free heterojunction for enhanced visible-light photocatalysis. *ACS applied materials & interfaces, 5*(21), 11392-11401.

Dos Santos, A. B., Cervantes, F. J., & Van Lier, J. B. (2007). Review paper on current technologies for decolourisation of textile wastewaters: perspectives for anaerobic biotechnology. *Bioresource technology, 98*(12), 2369-2385.

Ebrahimi, R., Hossienzadeh, K., Maleki, A., Ghanbari, R., Rezaee, R., Safari, M., . . . Yetilmezsoy, K. (2019). Effects of doping zinc oxide nanoparticles with transition metals (Ag, Cu, Mn) on photocatalytic degradation of Direct Blue 15 dye under UV and visible light irradiation. *Journal of Environmental Health Science and Engineering, 17*(1), 479-492.

Fan, J., & Freer, R. (1997). Varistor properties and microstructure of ZnO–BaO ceramics. *Journal of materials science, 32*(2), 415-419.

Fang, L., Ohfuji, H., Shinmei, T., & Irifune, T. (2011). Experimental study on the stability of graphitic C3N4 under high pressure and high temperature. *Diamond and Related Materials, 20*(5-6), 819-825.

Franco, P., Sacco, O., De Marco, I., Sannino, D., & Vaiano, V. (2020). Photocatalytic degradation of eriochrome black-T azo dye using Eu-doped ZnO prepared by supercritical antisolvent precipitation route: a preliminary investigation. *Topics in Catalysis, 63*(11), 1193-1205.

Gawade, V., Gavade, N., Shinde, H., Babar, S., Kadam, A., & Garadkar, K. (2017). Green synthesis of ZnO nanoparticles by using Calotropis procera leaves for the photodegradation

of methyl orange. *Journal of Materials Science: Materials in Electronics, 28*(18), 14033-14039.

Golmohammadi, M., Honarmand, M., & Ghanbari, S. (2020). A green approach to synthesis of ZnO nanoparticles using jujube fruit extract and their application in photocatalytic degradation of organic dyes. *Spectrochimica acta part A: molecular and biomolecular spectroscopy, 229*, 117961.

Güy, N., & Özacar, M. (2016). The influence of noble metals on photocatalytic activity of ZnO for Congo red degradation. *International Journal of Hydrogen Energy, 41*(44), 20100-20112.

Haibo, O., Feng, H. J., Cuiyan, L., Liyun, C., & Jie, F. (2013). Synthesis of carbon doped ZnO with a porous structure and its solar-light photocatalytic properties. *Materials Letters, 111*, 217-220.

Hakimi-Tehrani, M. J., Hassanzadeh-Tabrizi, S., Koupaei, N., Saffar-Teluri, A., & Rafiei, M. (2021). Facile thermal synthesis of g–C3N4/ZnO nanocomposite with antibacterial properties for photodegradation of Methylene blue. *Materials Research Express, 8*(12), 125002.

Hashimoto, K., Irie, H., & Fujishima, A. (2005). TiO2 photocatalysis: a historical overview and future prospects. *Japanese journal of applied physics, 44*(12R), 8269.

Hasnidawani, J., Azlina, H., Norita, H., Bonnia, N., Ratim, S., & Ali, E. (2016). Synthesis of ZnO nanostructures using sol-gel method. *Procedia Chemistry, 19*, 211-216.

Holkar, C. R., Jadhav, A. J., Pinjari, D. V., Mahamuni, N. M., & Pandit, A. B. (2016). A critical review on textile wastewater treatments: possible approaches. *Journal of environmental management, 182*, 351-366.

Isai, K. A., & Shrivatava, V. S. (2019). Photocatalytic degradation of methyl orange using ZnO and Fe doped ZnO: A comparative study. *Iranian Journal of Catalysis, 9*(3), 259-268.

Javid, M. A., Rafi, M., Ali, I., Hussain, F., Imran, M., & Nasir, A. (2016). Synthesis and study of structural properties of Sn doped ZnO nanoparticles. *Materials Science-Poland, 34*(4), 741-746.

Jayaram, P., Pradyumnan, P., & Karazhanov, S. Z. (2016). Micro-strain, dislocation density and surface chemical state analysis of multication thin films. *Physica B: Condensed Matter, 501*, 140-145.

Kadam, S. R., Mate, V. R., Panmand, R. P., Nikam, L. K., Kulkarni, M. V., Sonawane, R. S., & Kale, B. B. (2014). A green process for efficient lignin (biomass) degradation and hydrogen production via water splitting using nanostructured C, N, S-doped ZnO under solar light. *RSC advances*, *4*(105), 60626-60635.

Kajbafvala, A., Ghorbani, H., Paravar, A., Samberg, J. P., Kajbafvala, E., & Sadrnezhaad, S. (2012). Effects of morphology on photocatalytic performance of Zinc oxide nanostructures synthesized by rapid microwave irradiation methods. *Superlattices and Microstructures*, *51*(4), 512-522.

Kant, R. (2012). Textile dyeing industry an environmental hazard. J Nat Sci 4 (1): 22–26.

Karimi-Maleh, H., Fakude, C. T., Mabuba, N., Peleyeju, G. M., & Arotiba, O. A. (2019). The determination of 2-phenylphenol in the presence of 4-chlorophenol using nano-Fe3O4/ionic liquid paste electrode as an electrochemical sensor. *Journal of colloid and interface science*, *554*, 603-610.

Karthik, K., Raghu, A., Reddy, K. R., Ravishankar, R., Sangeeta, M., Shetti, N. P., & Reddy, C. V. (2022). Green synthesis of Cu-doped ZnO nanoparticles and its application for the photocatalytic degradation of hazardous organic pollutants. *Chemosphere*, *287*, 132081.

Karunakaran, C., & Dhanalakshmi, R. (2008). Semiconductor-catalyzed degradation of phenols with sunlight. *Solar energy materials and solar cells*, *92*(11), 1315-1321.

Katheresan, V., Kansedo, J., & Lau, S. Y. (2018). Efficiency of various recent wastewater dye removal methods: A review. *Journal of environmental chemical engineering*, *6*(4), 4676-4697.

Khalid, N., Hammad, A., Tahir, M., Rafique, M., Iqbal, T., Nabi, G., & Hussain, M. (2019). Enhanced photocatalytic activity of Al and Fe co-doped ZnO nanorods for methylene blue degradation. *Ceramics International*, *45*(17), 21430-21435.

Khan, I., Khan, S., Nongjai, R., Ahmed, H., & Khan, W. (2013). Structural and optical properties of gel-combustion synthesized Zr doped ZnO nanoparticles. *Optical Materials*, *35*(6), 1189-1193.

Khan, M. M., Adil, S. F., & Al-Mayouf, A. (2015). Metal oxides as photocatalysts (Vol. 19, pp. 462-464): Elsevier.

Khan, M. M., Lee, J., & Cho, M. H. (2014). Au@ TiO2 nanocomposites for the catalytic degradation of methyl orange and methylene blue: an electron relay effect. *Journal of Industrial and Engineering Chemistry, 20*(4), 1584-1590.

Khan, N. A., Bhadra, B. N., & Jhung, S. H. (2018). Heteropoly acid-loaded ionic liquid@ metal-organic frameworks: Effective and reusable adsorbents for the desulfurization of a liquid model fuel. *Chemical Engineering Journal, 334*, 2215-2221.

Kononenko, V., Repar, N., Marušič, N., Drašler, B., Romih, T., Hočevar, S., & Drobne, D. (2017). Comparative in vitro genotoxicity study of ZnO nanoparticles, ZnO macroparticles and ZnCl2 to MDCK kidney cells: Size matters. *Toxicology in Vitro, 40*, 256-263.

Kumar, M., Negi, K., Umar, A., & Chauhan, M. (2021). Photocatalytic and fluorescent chemical sensing applications of La-doped ZnO nanoparticles. *Chemical Papers, 75*(4), 1555-1566.

Kumar, N., Mittal, H., Alhassan, S. M., & Ray, S. S. (2018). Bionanocomposite hydrogel for the adsorption of dye and reusability of generated waste for the photodegradation of ciprofloxacin: a demonstration of the circularity concept for water purification. *ACS Sustainable Chemistry & Engineering, 6*(12), 17011-17025.

Kumar, N., Mittal, H., Reddy, L., Nair, P., Ngila, J. C., & Parashar, V. (2015). Morphogenesis of ZnO nanostructures: role of acetate (COOH−) and nitrate (NO 3−) ligand donors from zinc salt precursors in synthesis and morphology dependent photocatalytic properties. *RSC advances, 5*(48), 38801-38809.

Kumar, N., & Ray, S. S. (2018). Synthesis and functionalization of nanomaterials *Processing of Polymer-based Nanocomposites* (pp. 15-55): Springer.

Kumar, V., Gohain, M., Som, S., Kumar, V., Bezuindenhoudt, B., & Swart, H. C. (2016). Microwave assisted synthesis of ZnO nanoparticles for lighting and dye removal application. *Physica B: Condensed Matter, 480*, 36-41.

Kumaresan, N., Ramamurthi, K., Babu, R. R., Sethuraman, K., & Babu, S. M. (2017). Hydrothermally grown ZnO nanoparticles for effective photocatalytic activity. *Applied Surface Science, 418*, 138-146.

Lang, J., Wang, J., Zhang, Q., Li, X., Han, Q., Wei, M., . . . Yang, J. (2016). Chemical precipitation synthesis and significant enhancement in photocatalytic activity of Ce-doped ZnO nanoparticles. *Ceramics International, 42*(12), 14175-14181.

Li, N., Tian, Y., Zhao, J., Zhang, J., Zuo, W., Kong, L., & Cui, H. (2018). Z-scheme 2D/3D g-C3N4@ ZnO with enhanced photocatalytic activity for cephalexin oxidation under solar light. *Chemical Engineering Journal, 352*, 412-422.

Li, X., Ren, H., Zou, Z., Sun, J., Wang, J., & Liu, Z. (2016). Energy gap engineering of polymeric carbon nitride nanosheets for matching with NaYF 4: Yb, Tm: enhanced visible-near infrared photocatalytic activity. *Chemical Communications, 52*(3), 453-456.

Li, Z., Kong, C., & Lu, G. (2016). Visible photocatalytic water splitting and photocatalytic two-electron oxygen formation over Cu-and Fe-doped g-C3N4. *The Journal of Physical Chemistry C, 120*(1), 56-63.

Lianga, S. X. T., Wong, L. S., Lim, Y. M., Djearamanea, S., & Lee, P. F. (2020). Effects of Zinc Oxide nanoparticles on Streptococcus pyogenes. *South African Journal of Chemical Engineering, 34*(1), 63-71.

Liu, W., Wang, M., Xu, C., & Chen, S. (2012). Facile synthesis of g-C3N4/ZnO composite with enhanced visible light photooxidation and photoreduction properties. *Chemical Engineering Journal, 209*, 386-393.

Loh, K., Gaylarde, C., & Shirakawa, M. (2018). Photocatalytic activity of ZnO and TiO2 'nanoparticles' for use in cement mixes. *Construction and Building Materials, 167*, 853-859.

Lu, X., Xu, K., Tao, S., Shao, Z., Peng, X., Bi, W., . . . Wu, C. (2016). Engineering the electronic structure of two-dimensional subnanopore nanosheets using molecular titanium-oxide incorporation for enhanced photocatalytic activity. *Chemical science, 7*(2), 1462-1467.

Luo, Y., Deng, B., Pu, Y., Liu, A., Wang, J., Ma, K., . . . Dong, L. (2019). Interfacial coupling effects in g-C3N4/SrTiO3 nanocomposites with enhanced H2 evolution under visible light irradiation. *Applied Catalysis B: Environmental, 247*, 1-9.

Ma, S., Zhan, S., Xia, Y., Wang, P., Hou, Q., & Zhou, Q. (2019). Enhanced photocatalytic bactericidal performance and mechanism with novel Ag/ZnO/g-C3N4 composite under visible light. *Catalysis Today, 330*, 179-188.

Magesa, F., Wu, Y., Tian, Y., Vianney, J.-M., Buza, J., He, Q., & Tan, Y. (2019). Graphene and graphene like 2D graphitic carbon nitride: Electrochemical detection of food colorants and toxic substances in environment. *Trends in Environmental Analytical Chemistry, 23*, e00064.

Mahdavi, R., & Talesh, S. S. A. (2017). Sol-gel synthesis, structural and enhanced photocatalytic performance of Al doped ZnO nanoparticles. *Advanced Powder Technology, 28*(5), 1418-1425.

Mamba, G., Mamo, M. A., Mbianda, X. Y., & Mishra, A. K. (2014). Nd, N, S-TiO2 decorated on reduced graphene oxide for a visible light active photocatalyst for dye degradation: Comparison to its MWCNT/Nd, N, S-TiO2 analogue. *Industrial & Engineering Chemistry Research, 53*(37), 14329-14338.

Martin, D. J., Reardon, P. J. T., Moniz, S. J., & Tang, J. (2014). Visible light-driven pure water splitting by a nature-inspired organic semiconductor-based system. *Journal of the American Chemical Society, 136*(36), 12568-12571.

Mezohegyi, G., van der Zee, F. P., Font, J., Fortuny, A., & Fabregat, A. (2012). Towards advanced aqueous dye removal processes: a short review on the versatile role of activated carbon. *Journal of environmental management, 102*, 148-164.

Mirzaeifard, Z., Shariatinia, Z., Jourshabani, M., & Rezaei Darvishi, S. M. (2020). ZnO photocatalyst revisited: effective photocatalytic degradation of emerging contaminants using S-doped ZnO nanoparticles under visible light radiation. *Industrial & Engineering Chemistry Research, 59*(36), 15894-15911.

Modwi, A., Abbo, M., Hassan, E., Al-Duaij, O., & Houas, A. (2017). Adsorption kinetics and photocatalytic degradation of malachite green (MG) via Cu/ZnO nanocomposites. *Journal of environmental chemical engineering, 5*(6), 5954-5960.

Modwi, A., Khezami, L., Taha, K. K., Bessadok J, A., & Mokraoui, S. (2019). Photo-degradation of a mixture of dyes using Barium doped ZnO nanoparticles. *Journal of Materials Science: Materials in Electronics, 30*(15), 14714-14725.

Mohamed, R., & Shawky, A. (2018). CNT supported Mn-doped ZnO nanoparticles: simple synthesis and improved photocatalytic activity for degradation of malachite green dye under visible light. *Applied Nanoscience, 8*(5), 1179-1188.

Mojsov, K. D., Andronikov, D., Janevski, A., Kuzelov, A., & Gaber, S. (2016). The application of enzymes for the removal of dyes from textile effluents. *Advanced technologies, 5*(1), 81-86.

Murali, A., & Sohn, H. Y. (2018). Photocatalytic properties of plasma-synthesized zinc oxide and tin-doped zinc oxide (TZO) nanopowders and their applications as transparent conducting films. *Journal of Materials Science: Materials in Electronics, 29*(17), 14945-14959.

N'KONOU, K., Haris, M., Lare, Y., Baneto, M., & Napo, K. (2016). Effect of barium doping on the physical properties of zinc oxide nanoparticles elaborated via sonochemical synthesis method. *Pramana, 87*(1), 1-7.

Ngullie, R. C., Alaswad, S. O., Bhuvaneswari, K., Shanmugam, P., Pazhanivel, T., & Arunachalam, P. (2020). Synthesis and Characterization of Efficient ZnO/g-C3N4 Nanocomposites Photocatalyst for Photocatalytic Degradation of Methylene Blue. *Coatings, 10*(5), 500.

Nie, N., Zhang, L., Fu, J., Cheng, B., & Yu, J. (2018). Self-assembled hierarchical direct Z-scheme g-C3N4/ZnO microspheres with enhanced photocatalytic CO2 reduction performance. *Applied Surface Science, 441*, 12-22.

Omri, K., El Ghoul, J., Lemine, O., Bououdina, M., Zhang, B., & El Mir, L. (2013). Magnetic and optical properties of manganese doped ZnO nanoparticles synthesized by sol–gel technique. *Superlattices and Microstructures, 60*, 139-147.

Pan, H., Zhang, Y., Hu, Y., & Xie, H. (2020). Effect of cobalt doping on optical, magnetic and photocatalytic properties of ZnO nanoparticles. *Optik, 208*, 164560.

Pan, Y., Wang, Y., Zhou, A., Wang, A., Wu, Z., Lv, L., . . . Zhu, T. (2017). Removal of azo dye in an up-flow membrane-less bioelectrochemical system integrated with bio-contact oxidation reactor. *Chemical Engineering Journal, 326*, 454-461.

Patil, A. B., Patil, K. R., & Pardeshi, S. K. (2010). Ecofriendly synthesis and solar photocatalytic activity of S-doped ZnO. *Journal of hazardous materials, 183*(1-3), 315-323.

Pekakis, P. A., Xekoukoulotakis, N. P., & Mantzavinos, D. (2006). Treatment of textile dyehouse wastewater by TiO2 photocatalysis. *Water research, 40*(6), 1276-1286.

Prado, A. G., & Costa, L. L. (2009). Photocatalytic decouloration of malachite green dye by application of TiO2 nanotubes. *Journal of hazardous materials, 169*(1-3), 297-301.

Qamar, M. A., Javed, M., Shahid, S., Iqbal, S., Abubshait, S. A., Abubshait, H. A., . . . Ghaithan, H. M. (2021). Designing of highly active g-C3N4/Co@ ZnO ternary nanocomposites for the disinfection of pathogens and degradation of the organic pollutants from wastewater under visible light. *Journal of environmental chemical engineering, 9*(4), 105534.

Qi, K., Liu, S.-y., & Zada, A. (2020). Graphitic carbon nitride, a polymer photocatalyst. *Journal of the Taiwan Institute of Chemical Engineers, 109*, 111-123.

Qin, J., Yang, C., Cao, M., Zhang, X., Rajendran, S., Limpanart, S., . . . Liu, R. (2017). Two-dimensional porous sheet-like carbon-doped ZnO/g-C3N4 nanocomposite with high visible-light photocatalytic performance. *Materials Letters, 189*, 156-159.

Qu, X., Alvarez, P. J., & Li, Q. (2013). Applications of nanotechnology in water and wastewater treatment. *Water research, 47*(12), 3931-3946.

Raeisi-Kheirabadi, N., & Nezamzadeh-Ejhieh, A. (2020). A Z-scheme g-C3N4/Ag3PO4 nanocomposite: Its photocatalytic activity and capability for water splitting. *International Journal of Hydrogen Energy, 45*(58), 33381-33395.

Rajabi, H. R., Khani, O., Shamsipur, M., & Vatanpour, V. (2013). High-performance pure and Fe3+-ion doped ZnS quantum dots as green nanophotocatalysts for the removal of malachite green under UV-light irradiation. *Journal of hazardous materials, 250*, 370-378.

Rauf, M. A., & Ashraf, S. S. (2012). Survey of recent trends in biochemically assisted degradation of dyes. *Chemical Engineering Journal, 209*, 520-530.

Reza, K. M., Kurny, A., & Gulshan, F. (2017). Parameters affecting the photocatalytic degradation of dyes using TiO2: a review. *Applied Water Science, 7*(4), 1569-1578.

Robinson, T., McMullan, G., Marchant, R., & Nigam, P. (2001). Remediation of dyes in textile effluent: a critical review on current treatment technologies with a proposed alternative. *Bioresource technology, 77*(3), 247-255.

Rochat, J., Demenge, P., & Rerat, J. (1978). Toxicologic study of a fluorescent tracer: rhodamine B. *Toxicological European research. Recherche europeenne en toxicologie, 1*(1), 23-26.

Rodríguez-Couto, S., Osma, J. F., & Toca-Herrera, J. L. (2009). Removal of synthetic dyes by an eco-friendly strategy. *Engineering in Life Sciences, 9*(2), 116-123.

Rojas-Andrade, M. D., Chata, G., Rouholiman, D., Liu, J., Saltikov, C., & Chen, S. (2017). Antibacterial mechanisms of graphene-based composite nanomaterials. *Nanoscale, 9*(3), 994-1006.

Sadaiyandi, K., Kennedy, A., Sagadevan, S., Chowdhury, Z. Z., Johan, M., Bin, R., . . . Thamiz Selvi, R. (2018). Influence of Mg doping on ZnO nanoparticles for enhanced photocatalytic evaluation and antibacterial analysis. *Nanoscale research letters, 13*(1), 1-13.

Sajjad, M., Ullah, I., Khan, M., Khan, J., Khan, M. Y., & Qureshi, M. T. (2018). Structural and optical properties of pure and copper doped zinc oxide nanoparticles. *Results in Physics, 9,* 1301-1309.

Samadi, M., Zirak, M., Naseri, A., Khorashadizade, E., & Moshfegh, A. Z. (2016). Recent progress on doped ZnO nanostructures for visible-light photocatalysis. *Thin Solid Films, 605*, 2-19.

Samsudin, E. M., Goh, S. N., Wu, T. Y., Ling, T. T., Hamid, S. A., & Juan, J. C. (2015). Evaluation on the photocatalytic degradation activity of reactive blue 4 using pure anatase nano-TiO2. *Sains Malaysiana*, *44*(7), 1011-1019.

Sanad, M. F., Shalan, A. E., Bazid, S. M., & Abdelbasir, S. M. (2018). Pollutant degradation of different organic dyes using the photocatalytic activity of ZnO@ ZnS nanocomposite materials. *Journal of environmental chemical engineering, 6*(4), 3981-3990.

Sanchez, E., & Lopez, T. (1995). Effect of the preparation method on the band gap of titania and platinum-titania sol-gel materials. *Materials Letters*, *25*(5-6), 271-275.

Sanna, V., Pala, N., Alzari, V., Nuvoli, D., & Carcelli, M. (2016). ZnO nanoparticles with high degradation efficiency of organic dyes under sunlight irradiation. *Materials Letters, 162,* 257-260.

Sarro, M., Gule, N. P., Laurenti, E., Gamberini, R., Paganini, M. C., Mallon, P. E., & Calza, P. (2018). ZnO-based materials and enzymes hybrid systems as highly efficient catalysts for recalcitrant pollutants abatement. *Chemical Engineering Journal, 334,* 2530-2538.

Senapati, S., Srivastava, S. K., & Singh, S. B. (2012). Synthesis, characterization and photocatalytic activity of magnetically separable hexagonal Ni/ZnO nanostructure. *Nanoscale, 4*(20), 6604-6612.

Shamsadin-Azad, Z., Taher, M. A., Cheraghi, S., & Karimi-Maleh, H. (2019). A nanostructure voltammetric platform amplified with ionic liquid for determination of tert-butylhydroxyanisole in the presence kojic acid. *Journal of Food Measurement and Characterization, 13*(3), 1781-1787.

Sharma, N., Jandaik, S., Kumar, S., Chitkara, M., & Sandhu, I. S. (2016). Synthesis, characterisation and antimicrobial activity of manganese-and iron-doped zinc oxide nanoparticles. *Journal of Experimental Nanoscience, 11*(1), 54-71.

Sher, M., Javed, M., Shahid, S., Hakami, O., Qamar, M. A., Iqbal, S., . . . Baghdadi, H. B. (2021). Designing of highly active g-C3N4/Sn doped ZnO heterostructure as a photocatalyst for

the disinfection and degradation of the organic pollutants under visible light irradiation. *Journal of Photochemistry and Photobiology A: Chemistry, 418*, 113393.

Sher, M., Javed, M., Shahid, S., Iqbal, S., Qamar, M. A., Bahadur, A., & Qayyum, M. A. (2021a). The controlled synthesis of g-C_3N_4/Cd-doped ZnO nanocomposites as potential photocatalysts for the disinfection and degradation of organic pollutants under visible light irradiation.

Sher, M., Javed, M., Shahid, S., Iqbal, S., Qamar, M. A., Bahadur, A., & Qayyum, M. A. (2021b). The controlled synthesis of gC 3 N 4/Cd-doped ZnO nanocomposites as potential photocatalysts for the disinfection and degradation of organic pollutants under visible light irradiation. *RSC advances, 11*(4), 2025-2039.

Sher, M., Khan, S. A., Shahid, S., Javed, M., Qamar, M. A., Chinnathambi, A., & Almoallim, H. S. (2021). Synthesis of novel ternary hybrid g-C3N4@ Ag-ZnO nanocomposite with Z-scheme enhanced solar light-driven methylene blue degradation and antibacterial activities. *Journal of environmental chemical engineering, 9*(4), 105366.

Shi, Z., Zhang, Y., Shen, X., Duoerkun, G., Zhu, B., Zhang, L., . . . Chen, Z. (2020). Fabrication of g-C3N4/BiOBr heterojunctions on carbon fibers as weaveable photocatalyst for degrading tetracycline hydrochloride under visible light. *Chemical Engineering Journal, 386*, 124010.

Singh, J., Chang, Y.-Y., Koduru, J. R., & Yang, J.-K. (2018). Potential degradation of methylene blue (MB) by nano-metallic particles: A kinetic study and possible mechanism of MB degradation. *Environmental Engineering Research, 23*(1), 1-9.

Singh, R., Barman, P., & Sharma, D. (2017). Synthesis, structural and optical properties of Ag doped ZnO nanoparticles with enhanced photocatalytic properties by photo degradation of organic dyes. *Journal of Materials Science: Materials in Electronics, 28*(8), 5705-5717.

Sohrabnezhad, S., Pourahmad, A., & Radaee, E. (2009). Photocatalytic degradation of basic blue 9 by CoS nanoparticles supported on AlMCM-41 material as a catalyst. *Journal of hazardous materials, 170*(1), 184-190.

Sohrabnezhad, S., & Seifi, A. (2016). The green synthesis of Ag/ZnO in montmorillonite with enhanced photocatalytic activity. *Applied Surface Science, 386*, 33-40.

Solís, M., Solís, A., Pérez, H. I., Manjarrez, N., & Flores, M. (2012). Microbial decolouration of azo dyes: a review. *Process Biochemistry, 47*(12), 1723-1748.

Sun, S., Chang, X., Li, X., & Li, Z. (2013). Synthesis of N-doped ZnO nanoparticles with improved photocatalytical activity. *Ceramics International, 39*(5), 5197-5203.

Sundaram, I. M., Kalimuthu, S., & Ponniah, G. (2017). Highly active ZnO modified g-C3N4 Nanocomposite for dye degradation under UV and Visible Light with enhanced stability and antimicrobial activity. *Composites Communications, 5*, 64-71.

Svetlichnyi, V., Shabalina, A., Lapin, I., Goncharova, D., & Nemoykina, A. (2016). ZnO nanoparticles obtained by pulsed laser ablation and their composite with cotton fabric: Preparation and study of antibacterial activity. *Applied Surface Science, 372*, 20-29.

Tan, L.-L., Ong, W.-J., Chai, S.-P., & Mohamed, A. R. (2016). Visible-light-activated oxygen-rich TiO2 as next generation photocatalyst: Importance of annealing temperature on the photoactivity toward reduction of carbon dioxide. *Chemical Engineering Journal, 283*, 1254-1263.

Tang, L., Yu, J., Pang, Y., Zeng, G., Deng, Y., Wang, J., . . . Feng, H. (2018). Sustainable efficient adsorbent: alkali-acid modified magnetic biochar derived from sewage sludge for aqueous organic contaminant removal. *Chemical Engineering Journal, 336*, 160-169.

Tauc, J., Grigorovici, R., & Vancu, A. (1966). Optical properties and electronic structure of amorphous germanium. *physica status solidi (b), 15*(2), 627-637.

Uma, R., Ravichandran, K., Sriram, S., & Sakthivel, B. (2017). Cost-effective fabrication of ZnO/g-C3N4 composite thin films for enhanced photocatalytic activity against three different dyes (MB, MG and RhB). *Materials Chemistry and Physics, 201*, 147-155.

Varadavenkatesan, T., Lyubchik, E., Pai, S., Pugazhendhi, A., Vinayagam, R., & Selvaraj, R. (2019). Photocatalytic degradation of Rhodamine B by zinc oxide nanoparticles synthesized using the leaf extract of Cyanometra ramiflora. *Journal of Photochemistry and Photobiology B: Biology, 199*, 111621.

Verma, A. K., Dash, R. R., & Bhunia, P. (2012). A review on chemical coagulation/flocculation technologies for removal of colour from textile wastewaters. *Journal of environmental management, 93*(1), 154-168.

Vinitha, V., Preeyanghaa, M., Vinesh, V., Dhanalakshmi, R., Neppolian, B., & Sivamurugan, V. (2021). Two is better than one: Catalytic, sensing and optical applications of doped zinc oxide nanostructures. *Emergent Materials, 4*(5), 1093-1124.

Wang, J., Wang, X., Zhao, G., Song, G., Chen, D., Chen, H., . . . Wang, X. (2018). Polyvinylpyrrolidone and polyacrylamide intercalated molybdenum disulfide as adsorbents for enhanced removal of chromium (VI) from aqueous solutions. *Chemical Engineering Journal, 334*, 569-578.

Wang, S., Kuang, P., Cheng, B., Yu, J., & Jiang, C. (2018). ZnO hierarchical microsphere for enhanced photocatalytic activity. *Journal of Alloys and Compounds, 741*, 622-632.

Wang, X., Blechert, S., & Antonietti, M. (2012). Polymeric graphitic carbon nitride for heterogeneous photocatalysis. *Acs Catalysis, 2*(8), 1596-1606.

Wang, Y., Ge, S., Cheng, W., Hu, Z., Shao, Q., Wang, X., . . . Guo, Z. (2020). Microwave hydrothermally synthesized metal–organic framework-5 derived C-doped ZnO with enhanced photocatalytic degradation of rhodamine B. *Langmuir, 36*(33), 9658-9667.

Wang, Y., Jiang, W., Luo, W., Chen, X., & Zhu, Y. (2018). Ultrathin nanosheets g-C3N4@ Bi2WO6 core-shell structure via low temperature reassembled strategy to promote photocatalytic activity. *Applied Catalysis B: Environmental, 237*, 633-640.

Widiyandari, H., Umiati, N. A. K., & Herdianti, R. D. (2018). *Synthesis and photocatalytic property of Zinc Oxide (ZnO) fine particle using flame spray pyrolysis method.* Paper presented at the Journal of Physics: Conference Series.

Xing, H., Ma, H., Fu, Y., Xue, M., Zhang, X., Dong, X., & Zhang, X. (2015). Preparation of g-C3N4/ZnO composites and their enhanced photocatalytic activity. *Materials Technology, 30*(2), 122-127.

Yarahmadi, M., Maleki-Ghaleh, H., Mehr, M. E., Dargahi, Z., Rasouli, F., & Siadati, M. H. (2021). Synthesis and characterization of Sr-doped ZnO nanoparticles for photocatalytic applications. *Journal of Alloys and Compounds, 853*, 157000.

Yu, K. Q. B. C. J., & Ho, W. (2017). Review on the improvement of the photocatalytic and antibacterial activities of ZnO J. *Alloys Compd, 727*, 792-820.

Yu, W., Chen, J., Shang, T., Chen, L., Gu, L., & Peng, T. (2017). Direct Z-scheme g-C3N4/WO3 photocatalyst with atomically defined junction for H2 production. *Applied Catalysis B: Environmental, 219*, 693-704.

Yu, Z., Yin, L.-C., Xie, Y., Liu, G., Ma, X., & Cheng, H.-M. (2013). Crystallinity-dependent substitutional nitrogen doping in ZnO and its improved visible light photocatalytic activity. *Journal of colloid and interface science, 400*, 18-23.

Zahrim, A., & Hilal, N. (2013). Treatment of highly concentrated dye solution by coagulation/flocculation–sand filtration and nanofiltration. *Water resources and industry*, *3*, 23-34.

Zhang, G., Lan, Z.-A., Lin, L., Lin, S., & Wang, X. (2016). Overall water splitting by Pt/gC 3 N 4 photocatalysts without using sacrificial agents. *Chemical science*, *7*(5), 3062-3066.

Zhang, S., Su, C., Ren, H., Li, M., Zhu, L., Ge, S., . . . Cao, X. (2019). In-situ fabrication of g-C3N4/ZnO nanocomposites for photocatalytic degradation of methylene blue: synthesis procedure does matter. *Nanomaterials*, *9*(2), 215.

Zhong, Q., Lan, H., Zhang, M., Zhu, H., & Bu, M. (2020). Preparation of heterostructure g-C3N4/ZnO nanorods for high photocatalytic activity on different pollutants (MB, RhB, Cr (VI) and eosin). *Ceramics International*, *46*(8), 12192-12199.

Zhou, Y., Zhang, L., Huang, W., Kong, Q., Fan, X., Wang, M., & Shi, J. (2016). N-doped graphitic carbon-incorporated g-C3N4 for remarkably enhanced photocatalytic H2 evolution under visible light. *Carbon*, *99*, 111-117.

Zhu, P., Weng, Z., Li, X., Liu, X., Wu, S., Yeung, K., . . . Chu, P. K. (2016). Biomedical applications of functionalized ZnO nanomaterials: from biosensors to bioimaging. *Advanced Materials Interfaces*, *3*(1), 1500494.